

Special Section on Natural Products: Experimental Approaches to Elucidate Disposition Mechanisms and Predict Pharmacokinetic Drug Interactions

Mechanisms of Herb-Drug Interactions Involving Cinnamon and CYP2A6: Focus on Time-Dependent Inhibition by Cinnamaldehyde and 2-Methoxycinnamaldehyde[§]

Michael J. Espiritu, Justin Chen, Jaydeep Yadav, Michael Larkin, Robert D. Pelletier, Jeannine M. Chan, Jeevan B. GC, Senthil Natesan, and  John P. Harrelson

School of Pharmacy, Pacific University Oregon, Hillsboro, Oregon (M.J.E., M.L., J.P.H.); College of Pharmacy and Pharmaceutical Sciences, Washington State University, Spokane, Washington (J.C., J.B.G., S.N.); Amgen, Cambridge, Massachusetts (J.Y.); Department of Medicinal Chemistry, University of Washington, Seattle, Washington (R.D.P.); and Chemistry Department, Pacific University Oregon, Forest Grove, Oregon (J.M.C.)

Received April 7, 2020; accepted July 15, 2020

ABSTRACT

Information is scarce regarding pharmacokinetic-based herb-drug interactions (HDI) with *trans*-cinnamaldehyde (CA) and 2-methoxycinnamaldehyde (MCA), components of cinnamon. Given the presence of cinnamon in food and herbal treatments for various diseases, HDIs involving the CYP2A6 substrates nicotine and letrozole with MCA ($K_s = 1.58 \mu\text{M}$; Hill slope = 1.16) and CA were investigated. The time-dependent inhibition (TDI) by MCA and CA of CYP2A6-mediated nicotine metabolism is a complex process involving multiple mechanisms. Molecular dynamic simulations showed that CYP2A6's active site accommodates two dynamic ligands. The preferred binding orientations for MCA and CA were consistent with the observed metabolism: epoxidation, O-demethylation, and aromatic hydroxylation of MCA and cinnamic acid formation from CA. The percent remaining activity plots for TDI by MCA and CA were curved, and they were analyzed with a numerical method using models of varying complexity. The best-fit models support multiple inactivator binding, inhibitor depletion, and partial inactivation. Deconvoluted mass spectra indicated that MCA and CA modified CYP2A6 apoprotein with mass additions of 156.79 (142.54–171.04) and 132.67 (123.37–141.98), respectively, and it was unaffected by glutathione.

Heme degradation was observed in the presence of MCA (48.5% ± 13.4% loss; detected by liquid chromatography–tandem mass spectrometry). In the absence of clinical data, HDI predictions were made for nicotine and letrozole using inhibition parameters from the best-fit TDI models and parameters scaled from rats. Predicted area under the concentration–time curve fold changes were 4.29 (CA–nicotine), 4.92 (CA–letrozole), 4.35 (MCA–nicotine), and 5.00 (MCA–letrozole). These findings suggest that extensive exposure to cinnamon (corresponding to ≈ 275 mg CA) would lead to noteworthy interactions.

SIGNIFICANCE STATEMENT

Human exposure to cinnamon is common because of its presence in food and cinnamon-based herbal treatments. Little is known about the risk for cinnamaldehyde and methoxycinnamaldehyde, two components of cinnamon, to interact with drugs that are eliminated by CYP2A6-mediated metabolism. The interactions with CYP2A6 are complex, involving multiple-ligand binding, time-dependent inhibition of nicotine metabolism, heme degradation, and apoprotein modification. An herb-drug interaction prediction suggests that extensive exposure to cinnamon would lead to noteworthy interactions with nicotine.

Introduction

Cinnamon has been used for centuries as a spice and in traditional medicine (Ranasinghe et al., 2013). Large doses of cinnamon powder (1–10 g) have been reported for treating diabetes (Pham et al., 2007;

This work was supported by National Institutes of Health National Institute on Drug Abuse [Grant R15-DA042341] (to J.P.H. and J.M.C.) and National Institute of General Medical Sciences [Grant R15-GM131293] (to S.N.), the Pacific University School of Pharmacy Research Incentive grant to J.P.H., and Pacific Research Institute for Science and Mathematics grant to J.M.C.

<https://doi.org/10.1124/dmd.120.000087>.

[§]This article has supplemental material available at dmd.aspetjournals.org.

Crawford, 2009; Kirkham et al., 2009; Akilen et al., 2010), and the components of cinnamon are under investigation for a wide variety of other maladies, including inflammation (Hagenlocher et al., 2016; Schink et al., 2018; Cao et al., 2019; Cheng et al., 2020), multiple sclerosis (Pahan, 2015; Kundu et al., 2016), and pain (Burgess and Williams, 2010; Yokoyama et al., 2011; Weyer-Menkhoff and Lötsch, 2018, 2019). Considering its use in food (Friedman et al., 2000; Rietjens et al., 2020) and as a complementary treatment, there is potential for components in cinnamon to act as precipitants for herb-drug interactions (HDIs).

trans-Cinnamaldehyde (CA) and 2-methoxycinnamaldehyde (MCA) (Fig. 1) are present in cinnamon and are used for flavoring in the food

industry (Rietjens et al., 2020). CA is also often present in fluids for electronic nicotine delivery systems (Behar et al., 2016, 2018). Previously, we observed that CA is a time-dependent inhibitor of CYP2A6 (Chan et al., 2016). Compared with reversible inhibition, time-dependent inhibition (TDI) is especially concerning for HDI and drug-drug interactions (DDIs) because it can result in prolonged or irreversible inhibition due to long-lived metabolite/intermediate complexes (MICs) or enzyme inactivation by metabolites that covalently bind to either the apoprotein or heme prosthetic group essential for enzyme function (Mohutsky and Hall, 2014).

We hypothesized that MCA would inhibit CYP2A6 and investigated the kinetics and mechanisms of inhibition in comparison with CA. Traditionally, the replot method has been used to determine the TDI parameters, K_I and k_{inact} , from in vitro experiments. This involves graphing the percent remaining activity (PRA) and inactivation rates (k_{obs}) as a function of inhibitor concentration. K_I and k_{inact} are determined by fitting to the equation $k_{obs} = (k_{inact} \cdot [I]) / (K_I + [I])$ (Silverman, 1995). The approach is based on several assumptions: Michaelis-Menten/steady-state kinetics, irreversible inactivation, measurement of initial rates, and binding of a single substrate. In vitro-in vivo extrapolation (IVIVE) models use K_I and k_{inact} to assess the potential for DDIs and HDIs.

Previously, TDI parameters generated using the replot method and a static IVIVE model predicted a 3-fold change in nicotine AUC, with CA as a precipitant (Chan et al., 2016). However, the replot method overlooks several mechanistic complexities observed with P450 kinetics (e.g., multiple-ligand binding) and TDI (partial inactivation, reversible MIC formation). Oftentimes, only the linear portion of PRA plots is used to estimate K_I and k_{inact} , as longer incubations can result in nonlinear plots, which is indicative of mechanistic complexity (e.g., non-Michaelis-Menten kinetics), but also makes interpretation challenging with the replot method. Thus, the replot method can overpredict the likelihood for clinically relevant DDIs as a result of inaccuracies in parameter estimates, at least partially due to overlooking P450 TDI mechanistic complexity (Korzekwa et al., 2014). Numerical analysis was shown to lower error in parameter estimates in comparison with the replot method (Nagar et al., 2014).

Numerical analysis is a more recently developed approach for evaluating TDIs for DDI predictions (Yadav et al., 2020). It can account for diverse mechanistic complexities associated with P450 TDI and other factors (lipid partitioning). The mechanistic processes and kinetic models of varying complexity are described using ordinary differential equations, which are solved simultaneously to estimate inhibition parameters by fitting kinetic data to the models. Fit quality for individual models can provide evidence to support proposed mechanisms that contribute to a specific DDI/HDI scenario. Coupling information from numerical analysis with results from experiments designed to discover structure-based mechanistic information can further strengthen support for a proposed mechanism. Previously, using the standard replot method to analyze the TDI of CYP2A6 by MCA, the k_{obs} data fit best to a sigmoidal model, which provides evidence for the involvement of more complex mechanisms and atypical kinetics (manuscript under review). Here, we aimed to determine TDI parameters for the inhibition of nicotine metabolism by CA and MCA using numerical analysis, to

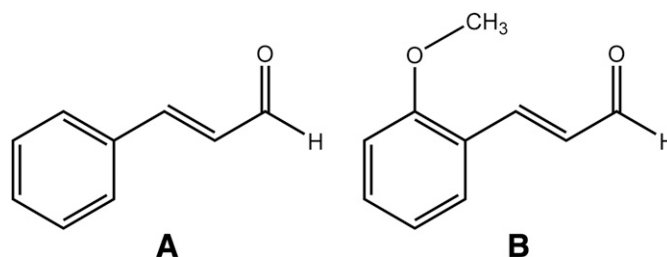


Fig. 1. (A) *trans*-cinnamaldehyde and (B) 2-methoxycinnamaldehyde.

assess potential mechanisms of inactivation, and to predict the potential for an HDI using IVIVE. We also evaluated the mechanisms of CYP2A6 interactions with CA and MCA using structure-based approaches. We analyzed binding affinity, inhibitor orientation, and inhibitor dynamics using spectral binding assays and molecular dynamic computational approaches. The inhibitory mechanism was investigated by measuring heme loss, which was observed previously with CA (manuscript under review), and apoprotein modification and by identifying CYP2A6-generated metabolites of MCA.

Materials and Methods

Materials. (–)-Cotinine, (±)-cotinine-D₃, *trans*-cinnamaldehyde, 2-methoxycinnamaldehyde, and reduced glutathione were obtained from Sigma-Aldrich. S-(–)-nicotine and NADPH tetrasodium salt were purchased from Alfa Aesar and EMD Chemicals, respectively. Pooled ($N = 50$ livers; 28 male and 22 female) human liver microsomes (HLMs) were obtained from Gibco. Human liver cytosol and NADPH solution A and solution B were obtained from Corning Life Sciences. High performance liquid chromatography columns were obtained from Phenomenex and Waters, as indicated below.

Expression and Purification of CYP2A6 and Rat Cytochrome P450 Reductase. CYP2A6 was expressed and purified as previously reported, with some slight modifications (Stephens et al., 2012; Chan et al., 2016). Spectral ligand binding assays, metabolite identification, apoprotein, and heme analysis experiments were conducted using modified recombinant human CYP2A6, which had an N-terminal transmembrane sequence truncation ($\Delta 2-23$) and a C-terminal His₄-tag. The recombinant protein was expressed from pKK2A6dH in DH5 α *Escherichia coli* with a 72-hour induction time in δ -amino levulinic acid-supplemented Terrific broth media. The protein was purified using Ni affinity chromatography, followed by carboxymethyl Sepharose cation exchange chromatography (Stephens et al., 2012). The detergent included in purification buffers was Brij L23. P450 content was determined from the carbon monoxide difference spectrum (Omura and Sato, 1962, 1964; Guengerich et al., 2009). Rat P450 reductase was expressed and purified as previously reported (Shen et al., 1989).

Molecular Dynamic Studies of CYP2A6-CA and CYP2A6-MCA Interactions. The three-dimensional structures of the ligand molecules CA and MCA were built, minimized, and geometry optimized in Molecular Operating Environment (MOE) (2019) from Chemical Computing Group (<https://www.chemcomp.com/Products.htm>). Charge calculation and atom types were assigned by the CHARMM General Force Field small-molecule parameterization module.

Molecular docking and dynamics studies were conducted using the published X-ray crystal structure of coumarin-bound CYP2A6 (PDB: 1Z10) (Yano et al., 2005; resolution 1.9 Å). Missing transmembrane helix residues 1–29 were

ABBREVIATIONS: AICc, Akaike's Information Criterion; AUC, area under the concentration-time curve; CA, *trans*-cinnamaldehyde; CHARMM Chemistry at Harvard Molecular Mechanics; CI confidence interval; DDI, drug-drug interaction; EII, multiple-inhibitor binding (double binding); $f_{m,CYP2A6}$, fraction of nicotine metabolized by CYP2A6; $f_{u,mic}$, unbound fraction in microsomes; $f_{u,p}$, unbound fraction in plasma; HDI, herb-drug interaction; HLM, human liver microsomes; IL, lipid partitioning; IVIVE, in vitro-in vivo extrapolation; LC-MS, liquid chromatography-mass spectrometry; LC-MS/MS, liquid chromatography-tandem mass spectrometry; M, indicates inhibitor depletion; MCA, 2-methoxycinnamaldehyde; MD, molecular dynamics; MIC, metabolite intermediate complex; MOE, Molecular Operating Environment; 8-MOP, 8-methoxypsoralen m/z mass to charge ratio; P450, cytochrome P450; PDB Protein Data Bank; PI, partial inactivation; PRA, percent remaining activity; rCYP2A6, recombinant CYP2A6; RMSD, root-mean-square deviation; TDI, time-dependent inhibition.

obtained as the FASTA sequence from UniProt (P11509-1) and constructed through homology modeling with MODELLER 9.19 (Šali and Blundell, 1993; Webb and Sali, 2016) using the intact X-ray crystal structure of the transmembrane domain of CYP51 [PDB: 5EQB (Monk et al., 2014)]. Of 100 models successfully generated by the software, the top-scoring model with the most favorable discrete optimized protein energy score was chosen for simulation. The fully constructed protein was prepared using the “Structure Preparation” module in MOE (missing atoms, residues, and H atoms were added; protonation states of residues were assigned using Protonate 3D within MOE) and then inserted and oriented within the 1-palmitoyl-2-oleoyl-sn-glycero-3-phosphocholine membrane using the Orientations of Proteins in Membranes web server (Lomize et al., 2012). The reoriented structure was measured to have a heme tilt angle and a transmembrane helix angle of 67.495° and 35.876° versus the bilayer normal (*z*-axis), respectively.

As guidance for docking CA and MCA to CYP2A6, 28 known CYP2A6 substrates or inhibitors with reported K_i values and binding modes were docked to identify the optimal combination of parameter settings within MOE for placement and refinement scoring (i.e., by reproducing the greatest number of crystal poses) for an induced-fit docking process. This pool included reversible inhibitors coumarin (PDB: 1Z10) and pilocarpine (PDB: 3T3Q), as well as irreversible inhibitors methoxsalen (PDB: 1Z11), aldrithiol (4,4'-dipyridyl disulfide, PDB: 2FDY), *N,N*-dimethyl(5-(pyridin-3-yl)furan-2-yl)methanamine (PDB: 2FDU), 5-(pyridin-3-yl)furan-2-yl)methanamine (PDB: 2FDW), and *N*-methyl(5-(pyridin-3-yl)furan-2-yl)methanamine (PDB: 2FDV). MMFF94X optimized force field for small molecules was chosen for docking within MOE. Usage of the London dG scoring function, the Triangle Matcher placement method, and Generalized-Born Volume Integral/Weighted Surface Area dG refinement scoring methods was found to reproduce the best poses for the studied molecules, as determined based on overlay root-mean-square deviation (RMSD) and adoption of the expected binding modes. Both CA and MCA were docked using the above set of parameters, and docked structures were used as the starting points for running all-atom MD simulations. In addition, a structure-based pharmacophore model (Fig. 2) was generated using the superpositioned crystal structures to obtain essential functional features. This model was used for selecting the best poses in addition to the docking scores.

All MD simulations were performed using the NAMD package (Phillips et al., 2005) under isothermal/isobaric NPT (number of particles; pressure constant;

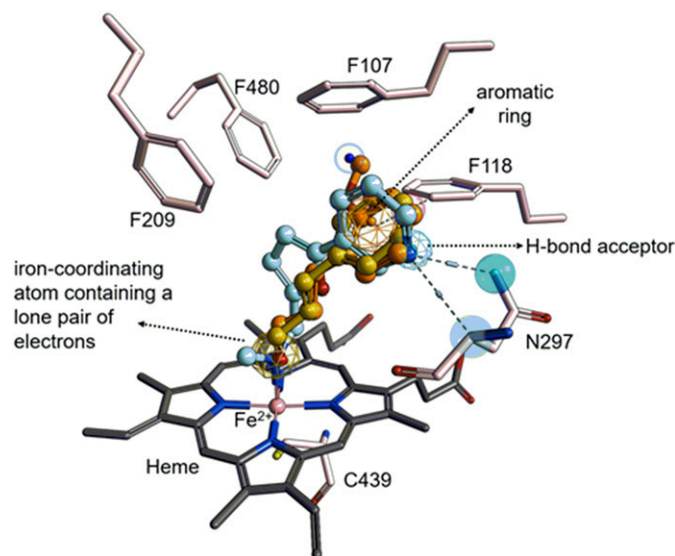


Fig. 2. Structure-based pharmacophore model generated from the superposition of published X-ray crystal structures of CYP2A6 bound to both reversible and irreversible inhibitors. The majority of the ligands had an H-bond acceptor (part of an aromatic ring) that made H-bond interaction with the amido -NH group of the binding site residue N297. Several phenylalanine residues, including F107, F118, F209, and F480, form an aromatic cage that makes π stacking interactions with the aromatic ring of the ligands. The distal end of ligands is in close proximity to the heme iron atom, coordinating through a lone pair of electrons carried by an electronegative atom such as *N*.

temperature constant) ensemble with periodic boundary conditions. The CHARMM36 force field (Huang and MacKerell, 2013), CHARMM General Force Field (Vanommeslaeghe et al., 2010, 2012; Vanommeslaeghe and MacKerell, 2012), and transferable intermolecular potential with 3 points (TIP3P) water model (Jorgensen et al., 1983) were employed for the protein and membrane, including monovalent ions, ligands, and solvent molecules, respectively. The CHARMM-GUI (Lee et al., 2016) membrane builder plug-in was used to construct the model membrane, which consisted of 90 and 105 1-palmitoyl-2-oleoyl-sn-glycero-3-phosphocholine lipids and 10 cholesterol molecules in the upper and lower leaflets, respectively. The CYP2A6-ligand complex oriented bilayer (Supplemental Fig. 1) was solvated with a minimum water thickness of 22.5 Å on each side.

The net charge of the membrane-CYP2A6-ligand complex systems was kept neutral (with 0.15 M KCl, i.e., 52 K^+ and 60 Cl^- ions) and subjected to a multistage minimization and equilibration protocol. In the first stage, the solvent molecules and ions were briefly minimized (2500 steps of steepest descent minimization followed by another 2500 steps of conjugate gradient method) to remove any bad contacts with the complexes. The rest of the system was position-restrained using a force constant of 100 kcal/(mol \times Å²). This step was followed by another 5000 steps of minimization of the whole solvated complex. The readjustment of membrane and solvent molecules to the potential field of the protein-ligand complex was achieved by subsequent heating and equilibration steps. The system was heated to a final temperature of 310 K in three steps; Langevin dynamics (Feller et al., 1995) was used in all stages to control the temperature using a collision frequency of 1.0 picoseconds⁻¹. The final solvent equilibration step was performed for 50 picoseconds under NPT conditions as above. The SHAKE algorithm (Ryckaert et al., 1977) was used to constrain bonds involving hydrogen, allowing a time step of 2 femtoseconds. Lennard-Jones and electrostatic interactions were calculated explicitly within a cutoff of 1.2 nm, and long-range electrostatic interactions were calculated by particle mesh Ewald summation (Ulrich et al., 1995). For both CA and MCA, the production simulation was carried out for 150 nanoseconds, and the trajectory files were written for every 5000 steps, resulting in 15,000 frames for each molecule.

The resulting trajectories were analyzed for potential H-bond interactions as well as the distance between ligand atoms and the heme iron atom using Hbonds plug-in Visual Molecular Dynamics software with the following criteria for the H-bonds: the distance between the donor atom (D) and the acceptor atom (A) is less than the cutoff distance of 3.5 Å, and the angle D-H-A is less than the cutoff angle of 40°.

Spectral Binding Studies with MCA and Purified CYP2A6. Samples of 1 μ M purified rCYP2A6 in 50 mM potassium phosphate buffer (pH = 7.4) were titrated with aliquots of MCA dissolved in DMSO. The final DMSO concentration in the titrations was kept below 1%. During the titration, solvent-only additions of equal volume (that is, equal to the volume added to the sample cuvette containing MCA) were added to a reference cuvette containing an identical protein sample. Difference spectra were recorded on a Shimadzu UV-visible 1601 spectrophotometer, and the Δ absorbance between the minimum and maximum was measured. Equilibrium dissociation constants (K_S) were determined from nonlinear least-squares fits to two equations: one-site specific ligand binding and specific binding with Hill slope using GraphPad Prism 8 (La Jolla, CA). Fits were compared using Akaike's Information Criterion (AICc). The experiment was repeated on three different days ($N = 3$), and each individual experiment was analyzed independently for comparison of model fits, as well as K_S and Hill coefficient determination.

CYP2A6-Mediated Metabolism of 2-Methoxycinnamaldehyde and Metabolite Identification by LC-MS. Purified rCYP2A6 (1 μ M) was reconstituted with rat cytochrome P450 reductase (1 μ M) and incubation buffer (100 mM potassium phosphate buffer; pH = 7.4) in microcentrifuge tubes. The incubations were preheated at 37°C for 5 minutes after the addition of MCA (200 μ M) and reduced glutathione (5 mM) to trap epoxide metabolites that could form. A 100 mM solution of MCA (in DMSO) was diluted in incubation buffer to make a 2 mM working solution, which was further diluted to the final concentration used in the incubations. The working stock of reduced glutathione was made in incubation buffer. Incubations (100 μ l final volume) were initiated with NADPH (1 mM), heated at 37°C for 1 hour in a water bath, and terminated with an equal volume of acetonitrile:methanol (1:1) and centrifuged. The supernatants were removed for LC-MS analysis, and those samples were analyzed using an AB Sciex 5600 TripleTOFTM system and mass defect filtering. Details of the method and data analysis are described in Supplemental Material 4.

Time-Dependent Inhibition of Nicotine Metabolism by CA and MCA in Human Liver Microsomes and Cytosol and LC-MS/MS Analysis of Nicotine and Cotinine. Time-dependent inhibition of CYP2A6 was tested using a standard two-step approach using pooled ($N = 50$) human liver microsomes (Yadav et al., 2018) with slight modifications. Briefly, 12 concentrations of either CA (0–1000 μM) or MCA (0–250 μM) were incubated at 37°C with a 5 mg/ml suspension of HLM in 100 mM potassium phosphate buffer (pH = 7.4) as a primary incubation. After 7 minutes of warming the primary incubation, the reaction was initiated by addition of NADPH regenerating system (final concentration 1.3 mM NADP⁺, 3.3 mM glucose-6-phosphate, 0.4 U/ml glucose-6-phosphate dehydrogenase, and 3.3 mM magnesium chloride). The NADPH regenerating system was used rather than NADPH salt to avoid the inhibition of P450 reductase at later time points by NADP⁺ accumulation. At specific time points, an aliquot (10 μl) of the primary incubation was added to 190 μl of secondary incubation. The secondary incubation consisted of nicotine (75 μM), NADPH (1 mM), and human liver cytosol (1 mg/ml). The conditions for the secondary incubation were developed based on previous studies of nicotine metabolism (Nakajima et al., 1996; Messina et al., 1997; Yamazaki et al., 1999; Le Gal et al., 2003). Since nicotine is metabolized by cytochrome P450 to nicotine- $\Delta^{1(5)}$ -iminium ion, which is further metabolized to cotinine by aldehyde oxidase (Murphy, 1973; Brandänge and Lindblom, 1979; Hukkanen et al., 2005);, cytosol was added to the secondary incubation to facilitate cotinine formation. The primary incubation was run for 0–90 minutes, and the secondary incubation was allowed to run for 10 minutes, followed by quenching with ice-cold acidified acetonitrile containing cotinine- D_3 as the internal standard. Each assay was conducted in triplicate. After centrifugation at 2000 rpm for 10 minutes, the supernatant was analyzed for cotinine by LC-MS/MS.

LC-MS/MS Analysis of Cotinine. Calibration curves were prepared in 0.25 mg/ml HLM in phosphate buffer (pH = 7.4) spiked with analyte standards, followed by precipitation with acetonitrile containing the internal standard cotinine- D_3 . The supernatant was analyzed with LC-MS/MS. For chromatographic separation of cotinine, a Phenomenex Synergi 4- μm Polar-RP 80-Å column (50 \times 2 mm) was used. The sample volume was 10 μl . An AB Sciex API 5500 LC-MS/MS system was used to analyze samples in positive ion mode using the following multiple reaction monitoring transitions: 176.979–80.016 m/z for cotinine and 179.985–80.022 m/z for cotinine- D_3 . LC-MS solvents consisted of 0.1 mM ammonium formate in water (pH = 4.0) as aqueous mobile phase (A) and 0.1% formic acid in acetonitrile as an organic mobile phase (B). The flow rate was 1 ml/min, with a gradient elution programmed from 5% to 95% B in 0.20 minutes maintained at 90% until 0.4 minutes and returned to initial condition at 0.8 minutes and maintained until 1.1 minutes. The total run time was 1.1 minutes, and the retention time was 0.61 minutes.

Microsomal Partitioning of CA and MCA. Nonspecific microsomal partitioning and human plasma protein binding were estimated using the model developed by Gao et al. (2008). The model was developed using molecular descriptors including calculated log P, calculated log D, pK_a, Kier connectivity, shape, and E-state indices, a subset of MOE descriptors, and a set of absorption, distribution, metabolism, and excretion (ADME) features. The statistical model was derived using the Cubist committee plus composite models, which is a tool for generating rule-based predictive models (Gao et al., 2008).

Model Fitting Using the Numerical Method and Estimate of TDI Parameters for CA and MCA. Cotinine concentrations obtained from the in vitro TDI experiments were converted to log (PRA) plots and further evaluated for model development. The concave upward curvature is indicative of either quasi-irreversible or partial inactivation, as shown previously (Nagar et al., 2014). Using the numerical method (Korzekwa et al., 2014; Nagar et al., 2014), kinetic models were fit to the data, and kinetic parameters were estimated. The initial estimates of the rate constants were obtained from analyzing the data as detailed in previous publications (Korzekwa et al., 2014; Nagar et al., 2014; Barnaba et al., 2016; Yadav et al., 2018, 2020). Association rate constants were fixed at 270 $\mu\text{M}^{-1} \text{min}^{-1}$ (Barnaba et al., 2016). For nicotine, the association (k_1) and dissociation rate constants (k_2) were fixed at 270 $\mu\text{M}^{-1} \text{min}^{-1}$ and 4050 min^{-1} , respectively, based on the reported K_M of nicotine (Yamazaki et al., 1999; Le Gal et al., 2003). Lipid partitioning was also incorporated in the models to account for microsomal partitioning (Yadav et al., 2019). The association rate constant for lipid was set at 2000 $\mu\text{M} \text{min}^{-1}$, and the dissociation rate constant was calculated using the following equation (Nagar and Korzekwa, 2017):

$$k_{off} = \frac{f_{u,mic} k_{on}}{1 - f_{u,mic}}$$

where k_{on} is the association rate constant, k_{off} is the dissociation rate constant, and $f_{u,mic}$ is the unbound fraction in the microsomes.

As previously mentioned, curvature in the PRA plots indicates either MIC formation or partial inactivation (Nagar et al., 2014). Curved PRA plots are also observed in cases of inhibitor depletion (Yadav et al., 2020). Several models were developed to capture the inactivation kinetics of CA. Further, a competitive inhibition model was fit to 0- and 60-minute time point data to obtain an initial estimate for K_I . A difference in initial estimates of K_I from 0 versus 60 minutes was indicative of multiple binding. As shown previously (Barnaba et al., 2016), MIC formation is a complex multistep process involving the formation of Fe^{+3} :carbene and Fe^{2+} :carbene. Hence, enzyme inactivation was modeled with three types of rate constants: e.g., in Fig. 8A, k_6 and k_{11} for Fe^{+3} :carbene formation, k_7 for the reformation of active enzyme, and k_8 for Fe^{2+} :carbene formation. The second type of quasi-irreversible model was also evaluated, which involved two steps denoted as k_6 and k_{11} for Fe^{+2} :carbene formation and k_7 for the reformation of active enzyme (Rodgers et al., 2018). Partial inactivation (PI) models were also tested, including partial inactivation with inhibitor depletion, double binding with partial inactivation, and the sequential formation of an intermediate leading to partial inactivation. The kinetic scheme for the simplest partial inactivation model is shown in Fig. 8C (Nagar et al., 2014).

Assuming rapid equilibrium, K_I values were estimated from ratios of association and dissociation rate constants. K_I obtained from the numerical method is the same as unbound $K_{I,u}$ ($K_{I,u} = K_I$) since lipid partitioning was incorporated in the model. Net k_{inact} was calculated using the net rate constant concept (Cleland, 1975). For MCA, net k_{inact} was calculated by using the following equation, which was derived using the net rate constant concept for the EII-PI-M-IL model:

$$k_{inact} = \frac{1}{\frac{1}{k_4} + \frac{1}{k_{11}} + \frac{k_6}{k_4}} + \frac{1}{\frac{1}{k_6} + \frac{k_4}{k_6 k_{11}}}$$

where

$$k_4' = \frac{k_4 k_{11}}{k_{10} + k_{11}}$$

Whereas for CA, k_{inact} was calculated by using the following equation for EII-MIC-M-IL:

$$k_{inact} = \frac{1}{\left(\frac{1}{k_6} + \frac{1}{k_8} + \frac{k_4}{k_6 k_{11}} + \frac{1}{k_4} + \frac{1}{k_{11}} + \frac{1}{k_8} + \frac{k_6}{k_4}\right)}$$

where

$$k_6' = \frac{k_6 k_8}{k_7 + k_8}, k_4' = \frac{k_4 k_{11}}{k_{10} + k_{11}}, k_{11}' = \frac{k_{11} k_8}{k_7 + k_8}$$

The replot method was also used to analyze the in vitro TDI data sets. The linear portion of the PRA plots was used to calculate the slopes (k_{obs}). The estimates of K_I and k_{inact} were obtained using the following replot equation:

$$k_{obs} = \frac{k_{inact} I}{K_{I,u} + I}$$

Although post hoc correction for lipid partitioning can lead to errors (Yadav et al., 2019), for comparison of replot and numerical method, unbound K_I was obtained by post hoc multiplying the K_I obtained from the above equation.

Parameter errors for net rate constants were calculated with error propagation for individual rate constants. AICc (Akaike, 1974) and adjusted R^2 were used to compare different models for each data set. Model fitting was conducted with Mathematica 11.3.0.0 (Wolfram Research, Champagne, IL) using the Non-linearModelFit function to fit the model to the data with PrecisionGoal = 10, finite difference derivatives with an order of 4, and 1/Y weighting.

Herb-Drug Interaction Prediction Using In Vitro-In Vivo Extrapolation. HDI predictions using $K_{I,u}$ and k_{inact} obtained from the numerical method were performed using the following mechanistic static equations (<https://www.fda.gov/media/134582/download>). HDI predictions were performed assuming no

substrate-dependent interactions by using nicotine and letrozole as CYP2A6 substrates. The estimated exposure of CA is between 8 and 275 mg (Friedman et al., 2000; Kirkham et al., 2009; Chan et al., 2016). Hence, a 275-mg dose was used to predict all the CA and MCA interactions with a dosing interval of 24 hours. For HDI predictions with MCA, K_{iu} and the net k_{inact} calculated (as shown above) were used. CYP2A6 is not known to be present in gut; therefore, only the systemic interaction was predicted for oral dosing of nicotine and letrozole. The following equations were used to predict AUC changes for the probe substrate dosed through the oral route:

$$\frac{AUC_i}{AUC} = \left(\frac{1}{\left(\frac{k_{deg,h}}{k_{deg,h} + \frac{I_{h,u} k_{inact}}{[I]_{h,u} + K_{iu}}} \right) \left(\frac{1}{1 + \frac{I_{h,u}}{K_{iu}}} \right) f_{m,CYP2A6} + (1 - f_{m,CYP2A6})} \right)$$

where AUC_i and AUC are the areas under the plasma concentration–time curve of the probe substrate in the presence and absence of the inactivator, respectively; $f_{m,CYP2A6}$ is the fraction of nicotine metabolized by CYP2A6; $[I]_h$ is the inactivator concentration in the hepatic portal vein (defined below); and $k_{deg,h}$ is the degradation rate constant of hepatic CYP2A6 (Yang et al., 2008). K_{iu} is the unbound competitive inhibition constant. K_{iu} was obtained from the literature by assuming competitive inhibition (Chan et al., 2016). $I_{h,u}$ was given by the following equations (Rostami-Hodjegan and Tucker, 2004; Obach et al., 2007):

$$I_h = \left(I_{max} + \frac{D k_a F_a F_g}{Q_h BP} \right)$$

$$I_{h,u} = f_{u,p} I_h$$

where I_{max} is the maximum concentration of the inactivator in plasma after oral dosing, D is the dose, F_a is the fraction absorbed, F_g is the fraction escaping gut metabolism, k_a is the first-order absorption rate constant, Q_h (1.5 l/h) is the hepatic blood flow, $f_{u,p}$ is the unbound fraction in the plasma, $f_{u,g}$ (assumed to be equal to 1) is the unbound fraction in the enterocyte, and BP is the blood-to-plasma partition ratio. Maximum unbound plasma concentration $I_{max,u}$ was given by the following equations

$$I_{max,u} = f_{u,p} \frac{I_{sys} k \tau}{1 - e^{-k \tau}}$$

where τ is the dosing interval, and k is elimination rate constant, which is calculated by the following equation:

$$k = \frac{CL_s}{V_{ss}}$$

where CL_s is the systemic clearance, and V_{ss} is the volume of distribution at steady state.

Average unbound systemic concentration $I_{sys,u}$ is the unbound average systemic inactivator concentration:

$$I_{sys,u} = f_{u,p} \left(\frac{F D}{\tau CL_s} \right)$$

where F is the bioavailability.

Human pharmacokinetic parameters for CA were predicted from rats to humans. Rat clearance and volume of distribution were obtained from the literature (Yuan et al., 1992). Human clearance was predicted using the following equation (Tang et al., 2007):

$$\frac{CL_{human}}{Kg} = 0.152 \frac{CL_{rat}}{Kg}$$

Volume from rats was scaled to human by using the following method (Caldwell et al., 2004):

$$V_{sshuman} = 0.6741 V_{ssrat}$$

For MCA, *in vitro* CL_{int} was predicted using an internal *in silico* Cubist-based model (Wenzel et al., 2019). The predicted CL_{int} was then scaled using biologic

scaling factors [microsomal protein per gram of liver = 45; liver weight = 1800 g (Davies and Morris, 1993) for a 70-kg human] assuming no extra hepatic clearance. *In vivo* CL for MCA was estimated using the well stirred model (Pang and Rowland, 1977) and the predicted *in vitro* CL_{int} . Volume of distribution for MCA was predicted using the Rodgers model (Rodgers and Rowland, 2006) using log P of 2.35, $f_{u,p}$ of 0.261, and pK_a of 14.

Inactivator pharmacokinetic parameters used for calculation of *in vivo* plasma inactivator concentrations are listed in Table 1.

LC-MS Search for Heme and Protoporphyrin IX Adducts with MCA and Metabolites of MCA. Purified rCYP2A6 (1 μ M) was reconstituted with rat cytochrome P450 reductase (1 μ M) and incubation buffer (100 mM potassium phosphate buffer; pH 7.4) in microcentrifuge tubes. The P450:reductase ratio for heme adduct analysis and heme degradation was based on the range of ratios used in previous studies (Raner et al., 1997; Kuo et al., 1999; Lin et al., 2005; Foti et al., 2011). The incubations were preheated at 37°C for 5 minutes after the addition of 200 μ M MCA, which was estimated to be a saturating concentration based on preliminary TDI experiments. Stock and working solutions of MCA were prepared as above for metabolite identification studies. Incubations were initiated with NADPH (1 mM final concentration) and heated at 37°C for 1 hour in the dark. The incubations were terminated with an equal volume of acetonitrile:methanol (1:1) with 1% formic acid, vortexed, and centrifuged. The supernatants were removed for LC-MS analysis, and those samples were analyzed using an AB Sciex 5600 TripleTOFTM system. Details of the method and analysis are described in Supplemental Material 5.

LC-MS/MS Analysis of Heme Degradation. Incubations were performed in microcentrifuge tubes in a 37°C water bath. Purified rCYP2A6 (400 pmol) and rat P450 reductase (400 pmol) were combined and left at room temperature for 10 minutes. Buffer (100 mM potassium phosphate; pH = 7.4) and MCA (80 μ M) were added and preincubated at 37°C for 5 minutes. The MCA concentration was selected for the purposes of comparison with CA from a previous study (Chan et al., 2016); also, it was estimated that 80 μ M approached enzyme saturation based on preliminary TDI experiments. NADPH (1 mM) was added to initiate the incubations, and the samples were heated at 37°C for 5 minutes. Incubations were terminated with an equal volume of acetonitrile, mixed with a vortex mixer, and centrifuged at 11,000g for 5 minutes. Enzyme-only controls (without MCA or NADPH) and controls without NADPH were prepared similarly. The supernatant was removed and was injected (50 μ l) onto a Phenomenex Kinetix C18 column (50 \times 2.1 mm; 2.6 μ m) using an AB Sciex Exion high performance liquid chromatography system interfaced with a 3500 triple quadrupole mass spectrometer. Heme was eluted using a gradient of 30% B to 95% B over 6 minutes (A = water/0.1% formic acid; B = acetonitrile/0.1% formic acid; 0.6 ml/min). Heme was detected by UV absorption at 405 nm and by ion intensity using multiple reaction monitoring at m/z = 616/557.2 (parent mass/transition state) in positive mode. Instrument parameters were as follows: ionspray voltage, 5500; declustering potential, 190 V; entrance potential, 10 V; collision energy, 54 eV; collision cell exit potential, 6 V; curtain gas, 30 psi; collision gas, 9 psi; ion source gas 1 and 2, 60 psi; temperature, 550°C. Nitrogen was used as the nebulizer, heater, and auxiliary gas. Heme loss was determined by comparing the change in peak area relative to the enzyme-only or enzyme and NADPH control areas, which were set to 100% of heme content. Statistical significance between individual data sets was determined using a two-tailed *t* test.

LC-MS/MS Analysis of the CYP2A6 Apoprotein. rCYP2A6 (60 pmol) and reductase (600 pmol) were combined and preincubated at room temperature for 10 minutes. The P450:reductase ratio was based on previous LC-MS/MS analyses of P450 apoprotein adducts with time-dependent inhibitors (Lin et al., 2005; Baer et al., 2007; Harrelson et al., 2012). Preliminary experiments showed that the detection and deconvolution of the protein envelope for rCYP2A6 was substantially better than reductase, so the relative amount of reductase used here was higher than the previous reports to improve the detection of reductase. Buffer (100 mM potassium phosphate, pH = 7.4) and MCA or CA (200 μ M) were added and preincubated at 37°C for 5 minutes. NADPH (1 mM) was added, and the samples were heated at 37°C for 20 minutes. A positive control containing 80 μ M 8-methoxypsoralen (8-MOP) was prepared in a similar fashion. All samples were compared with negative controls containing no inhibitor or no NADPH. A portion (10 μ l) of the incubation was analyzed on the aforementioned AB Sciex 3500 triple quadrupole LC-MS/MS system using a POROS 10 R1 column (2.1 mm internal diameter \times 100 mm; ThermoScientific). Protein was eluted using a gradient of 35% B to 55% B over 4 minutes (A = water/0.1% formic acid; B

TABLE 1
Pharmacokinetic parameters used for clinical HDI predictions

Parameters	Value
CA bioavailability (F)	0.22 ^d
MCA bioavailability (F)	0.22 ^b
CYP2A6 k_{deg}	0.019–0.036 h ⁻¹
k_a	6 ^c h ⁻¹
BP	1 ^c
CA fraction absorbed ($F_a * F_g$)	0.46 ^a
Systemic clearance (CL)	44.826 ^d l/h
Volume of distribution (V_{ss})	381.475 ^d l
MCA systemic clearance (CL)	40.68 l/h
MCA volume of distribution (V_{ss})	120.89 l
MCA fraction absorbed ($F_a * F_g$)	0.46 ^b
Nicotine $f_{m,CYP2A6}$	0.77 ^e
Letrozole $f_{m,CYP2A6}$	0.8 ^f
CA $I_{h,u}$ (μ M)	12.21
MCA $I_{h,u}$ (μ M)	14.39

^aObtained from rats and assumed to be the same in humans.

^bAssumed to be the same as CA.

^cBlood to plasma partition ratio is assumed.

^dCalculated from rats using allometry (see *Materials and Methods* section).

^eBenowitz and Jacob (1994).

^fEstimated from Sioufi et al. (1997), Murai et al. (2009), and Chan et al. (2016).

= acetonitrile/0.1% formic acid; 1.2 ml/min). Protein envelopes were detected using a Q1 scan in positive mode from 1000 to 2000 m/z. Instrument parameters were as follows: ionspray voltage, 4500; declustering potential, 170 V; entrance potential, 3 V; curtain gas, 30 psi; ion source gas 1 and 2, 60 psi; temperature, 25° C. Nitrogen was used as the nebulizer, heater, and auxiliary gas. After the spectra were obtained, deconvolution of the ion envelopes was undertaken by averaging the peak area corresponding to the retention time of CYP2A6 using the Biotool Kit plug-in in the AB Sciex Peakview software suite.

Results

Molecular Dynamics of CYP2A6-CA and CYP2A6-MCA Interactions. We performed molecular docking to predict the preferred binding modes of CA and MCA within the CYP2A6 binding site, followed by all-atom MD simulations to assess the dynamics and stability of the critical protein-ligand interactions. To guide the docking process, a structure-based pharmacophore model was developed using the available structural data on published crystal structures of several inhibitors bound to CYP2A6 (see *Materials and Methods* section). The sequence alignment and structure-based superposition revealed important structural features shared among these ligands (Fig. 2). Specifically, all bound substrates were found to overlay in a similar way, in which one end of the molecule occupied the distal axial heme coordination position, and the other was in close proximity to the N297 side chain amido group nitrogen. The majority of the ligands carried a complementary H-bond acceptor group, and all bound substrates contained an aromatic ring, likely to be essential for engaging in π - π interactions with the aromatic side chains of several phenylalanine residues, including F118, F107, F209, F480, and F111. Our docking procedure used the coordinates of these superpositioned ligands as well as the consensus features as a template for guided docking. The best-docked poses generated for CA and MCA were in close agreement with the expected pose, with their aldehyde groups pointing toward the heme iron atom and the benzene ring in close proximity to N297.

The trajectory analyses of 150-nanosecond-long MD simulations for each ligand revealed the major binding modes, critical interactions, and dynamic nature of these molecules within the binding pocket. After approximately 2 nanoseconds into the simulation, CA changed from its initial docked pose and reoriented to a more stable pose in which its carbonyl oxygen engaged in H-bonding with N297 (Fig. 3A). This binding orientation of CA lasted for 76.6 nanoseconds (51.07% of 150

nanoseconds total). The H-bond interaction between the oxygen atom of CA and the side chain amido group of N297 was characterized by an average distance of \sim 2.93 Å and an angle of \sim 142° (Supplemental Fig. 2A). CA was also stabilized in this pose by a T-shaped π stacking with F209 (an average distance of \sim 3.48 Å). The H-bond with N297 was maintained for the remainder of the simulation, although the entry and binding of a water molecule that began to coordinate with the heme iron (at \sim 77 nanoseconds) pushed CA's aromatic end toward the phenylalanine-rich region (Fig. 3B). The π stacking interaction with F107 stabilized CA in this configuration for the rest of the simulation. The dynamic nature of CA within the binding pocket was characterized by the RMSD values in reference to the initial docked pose, calculated for the entire simulation time (Supplemental Fig. 2B).

Interestingly, the MCA molecule also shifted from its docked pose to an entirely different pose after approximately 8 nanoseconds into the simulation. Initially, the aldehyde group was pointing toward the heme iron, and the methoxyl oxygen was in contact with N297 engaging in an H-bond interaction (Fig. 4A). As with CA, the rearrangement was prompted by the entry of several water molecules near N297. This caused MCA to reorient itself to a different pose (Fig. 4B). In this stable pose, which lasted for more than 80% of the total simulation, the oxygen atom of the aldehyde group was engaged in a water-mediated interaction with N297, whereas the phenyl ring was in close proximity to the heme iron atom (\sim 2.96 Å, Supplemental Fig. 3A). Likewise, the overall dynamics of MCA within the binding pocket was calculated as RMSD values in reference to the initial docked pose for the entire simulation time (Supplemental Fig. 3B).

Multiple-ligand binding and cooperative kinetics (i.e., non-Michaelis-Menten) are widely observed with xenobiotic-metabolizing P450s (Atkins, 2005). Homotropic and heterotropic cooperative kinetic behavior has been observed for CYP2A6-mediated metabolism; for example, the binding of multiple xylene ligands modulated substrate motion and product selectivity (Harrelson et al., 2008). To investigate the possible cooperativity effects in binding for each of the two ligands, we prepared an analogous system with a second copy of the molecule (ligand 2) docked in close proximity to the already-docked CYP2A6-ligand complex. This was possible because of the volume of the binding pocket, which allowed enough space left after the first molecule (ligand 1) was docked. We performed MD simulations on these systems to investigate the effect of dual ligands on the binding pose and interactions of CA and MCA to CYP2A6. For the cinnamaldehyde simulation, the second ligand molecule (CA-2) is less stable than the first one (CA-1) and experienced more dynamic behavior, retaining its initial pose for only 3.24 nanoseconds before its carbonyl oxygen began to respond to the presence of a cluster of water molecules near an access channel by the residue T482 (Fig. 5). At the same time, CA-1 was bound in a highly similar pose to the docked pose, with its aromatic group oriented toward the phenylalanine-rich region. This pose was maintained for 64 nanoseconds (\sim 43% of the total simulation time) by a network of π stacking interactions from F118, F107, and F209. The aromatic ring of CA-2 was oriented such that it made an edge-edge π - π interaction with F209 (Fig. 5). After \sim 65 nanoseconds, the entry of water molecules propelled CA-2 toward the heme, its aromatic ring colliding with the polar end of CA-1. The torque felt by CA-1 displaced the aldehyde group toward N297, and the electrostatic force eventually stabilized the CA-1 in this pose for the remainder of the simulation (86 nanoseconds, 57.48% of the total simulation time) (Supplemental Fig. 2D).

In the case of MCA, the docked pose of MCA-1 was maintained for a much longer duration, held for 58.84 nanoseconds (39% of the simulation time), with supportive contribution from the second

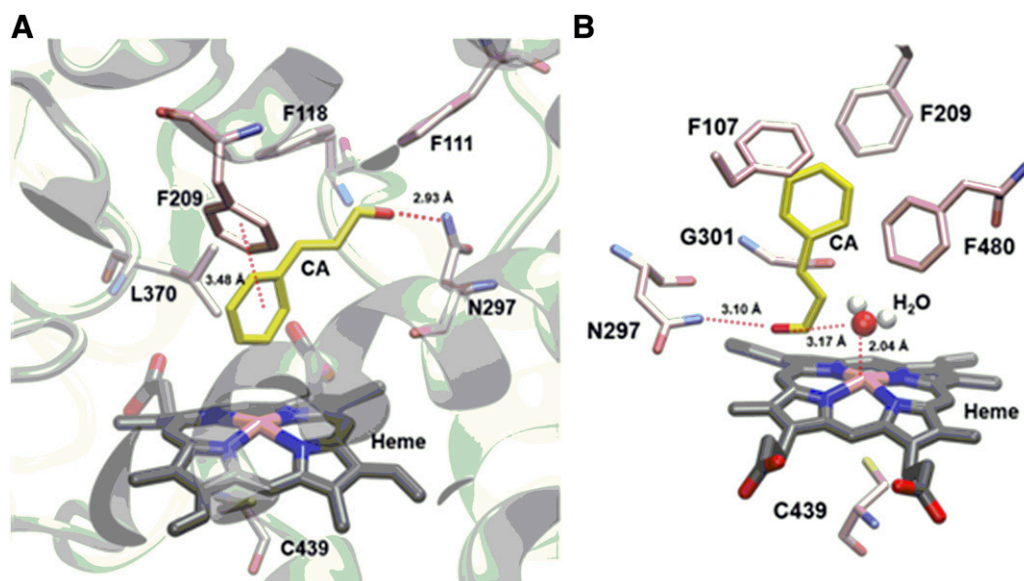


Fig. 3. The major binding poses and critical interactions of CA within the binding site of CYP2A6. (A) CA changed its binding pose from the initial docked pose after 2 nanoseconds and assumed an entirely different orientation in which the carbonyl oxygen was engaged in an H-bond with N297. (B) The entry of a water molecule altered CA binding and slightly increased the H-bond length but increased aryl-aryl interactions with several phenylalanine residues.

molecule, MCA-2 (Supplemental Fig. 3, C and D). Interestingly, the slight rearrangement involves a rotation that places its methoxyl oxygen in an optimal position for hydrogen bonding with N297, while its aldehyde group continued to maintain its positioning above the heme iron (Fig. 6A). This interaction was maintained for 108 nanoseconds until the long-lasting water-mediated interaction between MCA-2 with T309 and T305 finally broke, freeing the MCA-2 carbonyl oxygen, which became attracted to the water cluster at the opposing end of the site (Fig. 6). Despite a slight displacement, MCA-1 continued to be stabilized by the electrostatic interaction of the methoxyl oxygen with N297 and the π interaction of the aromatic benzene ring with F118 (Fig. 6B). Increased dynamics of both ligands

in the site were seen shortly after 108 nanoseconds and until 135 nanoseconds, after which MCA-1 steadily reoriented back to the favorable predominant pose (pose assumed between 23 and 100 nanoseconds), which was maintained through 150 nanoseconds (Supplemental Fig. 3D).

Spectral Analysis of MCA Binding to Human CYP2A6. Spectral binding studies were conducted on three different days with rCYP2A6 to evaluate the binding affinity between MCA and CYP2A6 (Fig. 7). The spectra indicated that MCA is a type I ligand of CYP2A6, consistent with a compound deficient in sp^2 hybridized nitrogen atoms. The data were fit to two different models in Prism: one-site specific ligand binding and specific binding with Hill slope. Specific binding with Hill slope

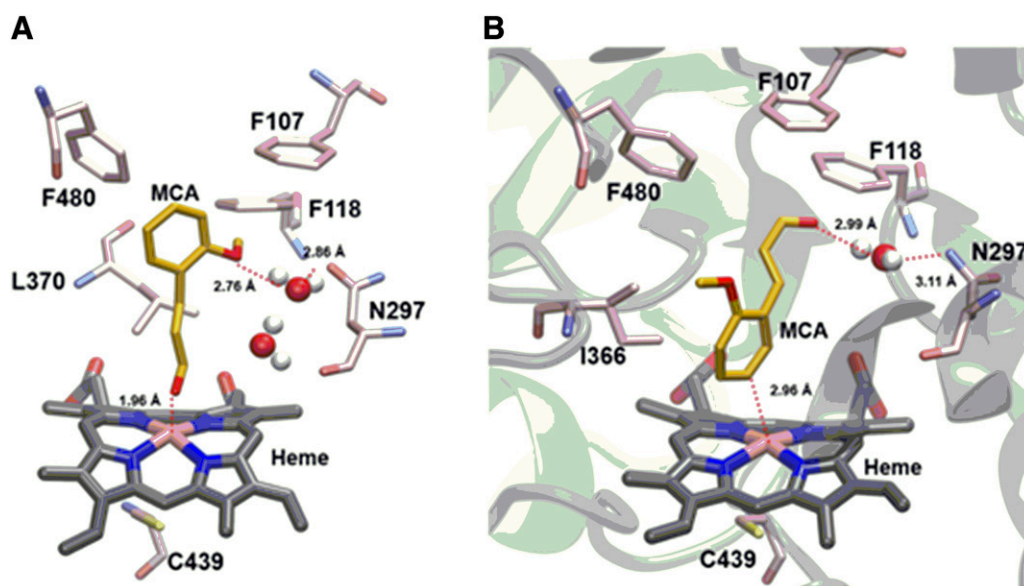


Fig. 4. The major binding poses and critical interactions of MCA within the binding site of CYP2A6. (A) MCA changed its binding pose from the initial docked pose after 8 nanoseconds and assumed a slightly different orientation in which the methoxyl oxygen was engaged in an H-bond with N297 through a water molecule. (B) The entry of several water molecules flipped the orientation of MCA to an entirely different binding mode in which the aromatic ring came close to the heme iron atom. The carbonyl oxygen was engaged in a water-mediated H-bond interaction with N297.

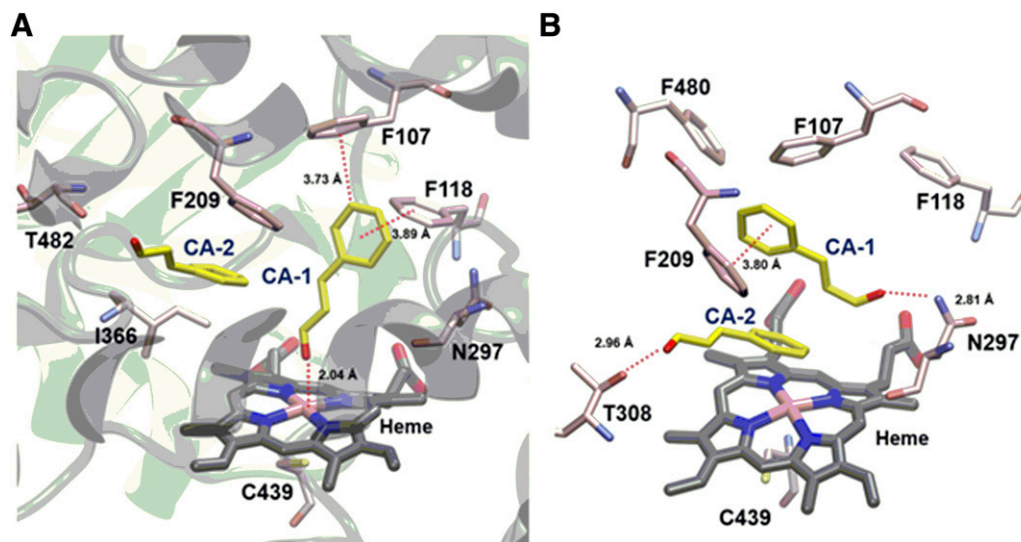


Fig. 5. The major binding poses and critical interactions of two CA molecules bound to CYP2A6 at the same time. (A) CA-1 was stabilized in its initial docked pose for 60 nanoseconds, after which it changed its orientation in which the carbonyl oxygen that was initially in close proximity to the heme iron shifted to near N297 and formed an H-bond. (B) The second CA molecule moved toward the heme and positioned its aromatic ring in π stacking with F209, which is also in π - π interaction with CA-1. The carbonyl oxygen atom of CA-2 made an H-bond interaction with T308, although the interaction was dynamic in nature (see Supplemental Fig. 2C).

was the preferred model for all experiments based on differences in AICc. The probabilities for correctness in comparison with the one-site specific binding model were 99.93%, 62.97%, and 99.99%, with AICc differences of 14.11, 1.06, and 17.73, respectively. Fits to the model using specific binding with Hill slope generated a $K_S = 1.58 \mu\text{M}$ (S.D. = 0.03; 95% CI = 1.50–1.66; $N = 3$), a Hill slope = 1.16 (S.D. = 0.26; 95% CI = 0.50–1.81), and R^2 values of 0.9993, 0.9971, and 0.9994. R^2 values for the one-site specific binding model were 0.9949, 0.9970, and 0.9958.

CYP2A6-Mediated Metabolism of 2-Methoxycinnamaldehyde and Metabolite Identification by LC-MS. The metabolism of MCA was investigated using a reconstituted system with rCYP2A6 and P450 reductase (i.e., the same system used for heme analysis). Based on parent masses, fragmentation patterns, and mass defect analysis, three metabolites were detected from CYP2A6-mediated oxidative metabolism: demethylation of the 2-methoxy group, trapped as a glutathione conjugate ($m/z = 456.1428$ and 456.1436); epoxidation of the double bond between the α - and β -carbons ($m/z = 178.0630$); and ring hydroxylation ($m/z = 178.0630$). Epoxidation and ring hydroxylation were clearly delineated from each other through their respective fragmentation patterns and the mass defect of their fragments. Epoxidation resulted in a unique 146.0362 m/z fragment corresponding to a 3,6-dioxatricyclo[5.4.0.0.2,4]undeca-1(7),4,8,10-tetraene, and the tandem mass spectrometry spectra were devoid of the acrolein fragment seen in the spectra of both MCA and the ring hydroxylated metabolite, indicating side chain modification. The epoxide was also found trapped as a glutathione conjugate, resulting in ring opening and side chain hydroxyl formation ($m/z = 486.1531$). The ring hydroxylation metabolite was deduced from several fragments, which clearly eliminated the possibility of the presence of hydroxylation on either the side chain or the methyl group. Discerning fragments included the parent minus acetaldehyde ($m/z = 136.052$), the parent minus a methyl group ($m/z = 163.0388$), and acrolein ($m/z = 55.0171$). Representative liquid chromatography traces and mass spectra with fragment structures are available in the Supplemental Material 6.

Time-Dependent Inhibition of CYP2A6-Mediated Nicotine Metabolism by CA and MCA. Several kinetic models were developed

for both of the inactivators to capture the inactivation kinetics. The best-fit model was chosen based on AICc values, R^2 , and residual analysis. Curved PRA plots indicated either formation of MIC or partial inactivation; hence, both types of models were tested for CA. Although both quasi-irreversible and partial inactivation models result in curved PRA plots, the shapes for both of the mechanisms are different. For quasi-irreversible inactivation, the terminal plateau region is inhibitor concentration-dependent and concentration-independent for partial inactivation (Nagar et al., 2014). Notably, at later time points, activity recovery at lower inhibitor concentrations suggested significant inhibitor loss during the preincubation phase. Graphs of the predicted depletion of each inhibitor are available in Supplemental Figs. 4 and 5.

As expected, Michaelis-Menten models with and without inhibitor depletion gave a poor fit (data not shown, AICc for the Michaelis-Menten model with inhibitor depletion was -337 , and AICc for the Michaelis-Menten model without inhibitor depletion was -295). Preliminary analysis suggested partial inactivation as a better model than a quasi-irreversible model (AICc -536 vs. -511). The single-binding quasi-irreversible with inhibitor depletion model (MIC-M-IL) did not result in a convergence, because of a lack of a reasonable estimate of the second step of inactivation (represented as k_8 in Fig. 8A). Therefore, a sensitivity analysis was also performed with a range of k_8 values between 0 and $0.005 \text{ minutes}^{-1}$. Equally good fits were observed when values were fixed at $\leq 0.005 \text{ minutes}^{-1}$. Hence, $0.005 \text{ minutes}^{-1}$ was considered as an upper limit and 0 minutes^{-1} as the lower limit for k_8 . Since the model fitting for an EII-MIC-M-IL model showed that $k_8 \rightarrow 0$, the second type of MIC model, in which inactivation was modeled as two steps, was also tested (Fig. 8B). The modified quasi-irreversible model gave a reasonable fit with an AICc = -495 (data not shown).

Double-binding models were also investigated both with quasi-irreversible and partial inactivation models. A double-binding model along with inhibitor depletion (EII-MIC-M-IL) improved the fit as compared with a single-binding quasi-irreversible model, but not for a partial inactivation model. Addition of a second binding to the partial inactivation model did not improve the model fit in comparison with the single-binding model PI-M-IL (data not shown). AICc and adjusted R^2

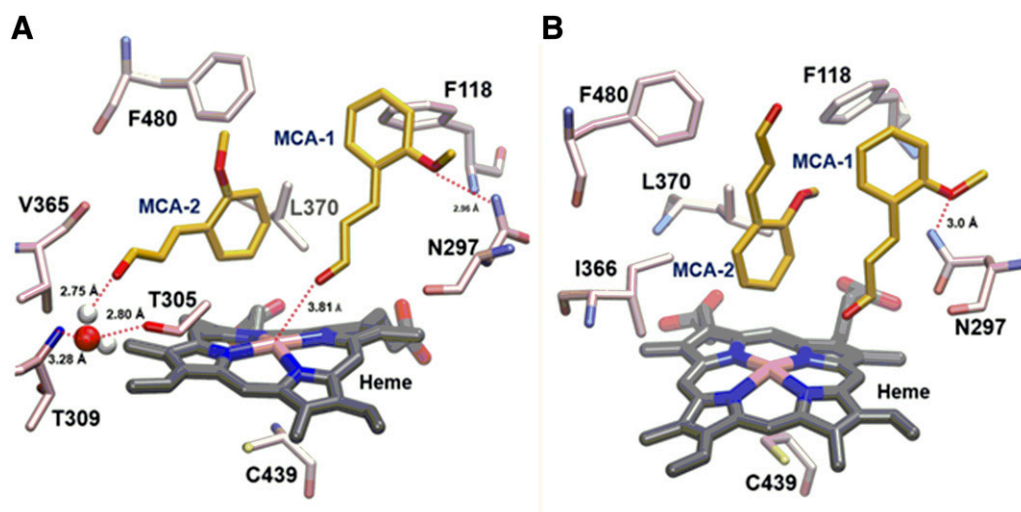


Fig. 6. The major binding poses and critical interactions of two MCAs bound to CYP2A6 at the same time. (A) MCA-1 was stabilized in its initial docked pose in which the methoxyl oxygen group was engaged in an H-bond with N297. (B) After 100 nanoseconds, the second MCA molecule moved toward the heme and pushed the carbonyl oxygen away from the heme iron. The carbonyl oxygen atom of MCA-2 reoriented its position toward the aromatic cage (see Supplemental Fig. 3, C and D).

for the EII-MIC-M-IL model were -528.557 and 0.99872 , respectively, whereas for PI-M-IL, the AICc and adjusted R^2 were -536.417 and 0.99881 , respectively. The fits for all three models are shown in Fig. 8. Figure 8D shows that the EII-MIC-M-IL model fit the CA data set assuming $k_8 = 0.005 \text{ minutes}^{-1}$. The k_{inact} for CA with an upper limit of k_8 as $0.005 \text{ minutes}^{-1}$ was estimated to be $0.0032 \pm 0.001 \text{ minutes}^{-1}$ for the EII-MIC-M-IL model (Table 2). The k_{inact}

for CA was found to be 0.023 ± 0.012 and $0.1 \pm 0.01 \text{ minutes}^{-1}$ for the EII-MIC-M-IL model and PI-M-IL model, respectively. The estimated rate constants for all the models were well defined (Supplemental Table 1). However, the propagation of errors to calculate the net k_{inact} value resulted in a high error (0.023 ± 0.012 and $0.0032 \pm 0.001 \text{ minutes}^{-1}$). The estimates of $K_{\text{I,u}}$ for CA with different models are shown in Table 2. The estimates of individual rate constants for each model fit are provided in Supplemental Table 1. All three models were able to capture the concave upward curvature observed in the PRA plots reasonably well (Fig. 8, D–F). However, AICc differences suggested PI-M-IL as the better model.

The MCA data set also gave nonlinear PRA plots suggesting either quasi-irreversible or partial inactivation. Preliminary results suggested that inhibitor loss was required to capture the inactivation kinetics. Hence, partial inactivation with inhibitor depletion (PI-M-IL) and quasi-irreversible with inhibitor depletion models (MIC-M-IL) were tested. It was found that a partial inactivation model with inhibitor depletion (PI-M-IL) gave a better fit as compared with a quasi-irreversible model with inhibitor depletion (MIC-M-IL) (Table 3; AICc -608 vs. -583). Further, analysis of the data set suggested a K_{I} value of $\sim 125 \mu\text{M}$, which is inconsistent with the competitive inhibition observed after inhibitor dilution ($K_{\text{I}} \sim 2.5 \mu\text{M}$). Therefore, double-binding models with either quasi-irreversible or partial inactivation were also evaluated.

Biphasic kinetics is observed when $k_{\text{inact}2} > k_{\text{inact}1}$, and inhibition of inactivation is observed when $k_{\text{inact}1} > k_{\text{inact}2}$ (Nagar et al., 2014). Preliminary analysis of MCA data sets suggested $K_{\text{I}2} > K_{\text{I}1}$ and $k_{\text{inact}2} > k_{\text{inact}1}$; however, fitting with constraints on $K_{\text{I}1}$ and $k_{\text{inact}2}$ did not result in model convergence. Using the standard replot method and linear sections of the PRA plot suggested biphasic kinetics with lack of saturation for the second binding. In general, it is difficult to estimate net inactivation and $K_{\text{I}2}$ if $k_{\text{inact}1} \ll k_{\text{inact}2}$ and $K_{\text{I}2} \gg K_{\text{I}1}$ and/or inhibitor concentrations do not cover the saturation range for $K_{\text{I}2}$. As suggested previously, the slower k_{inact} is more difficult to parameterize (Nagar et al., 2014). Therefore, optimization steps were followed (Nagar et al., 2014). Briefly, $K_{\text{I}1}$ was estimated from the 0-minute incubation time. The value of $k_{\text{inact}2}$ was estimated from the standard replot method. $K_{\text{I}2}$ and $k_{\text{inact}1}$ were optimized while constraining $k_{\text{inact}2}$ and $K_{\text{I}1}$. However, the model was unable to parameterize the second binding K_{I} . Manual optimization showed that the objective

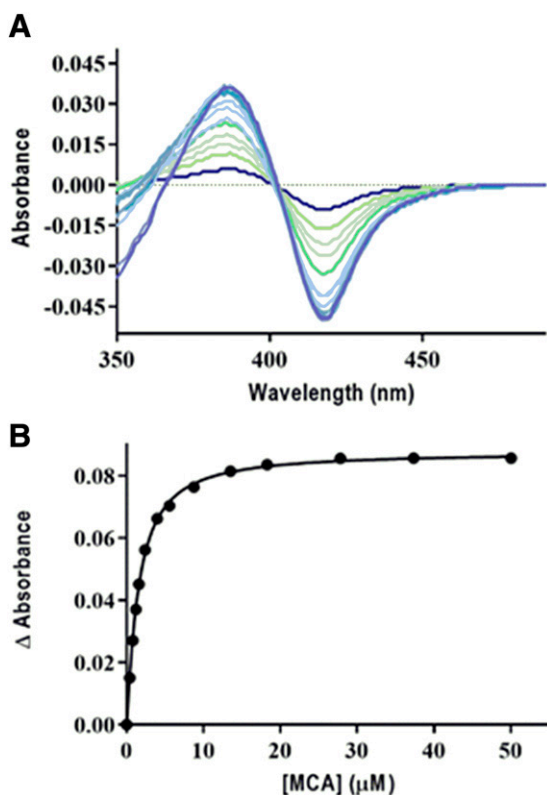


Fig. 7. (A) Representative binding difference spectra of purified rCYP2A6 with increasing concentrations of MCA. (B) A representative curve generated from fitting changes in absorbance ($A_{386 \text{ nm}} - A_{418 \text{ nm}}$) to model using specific binding with Hill slope, as a function of MCA concentration.

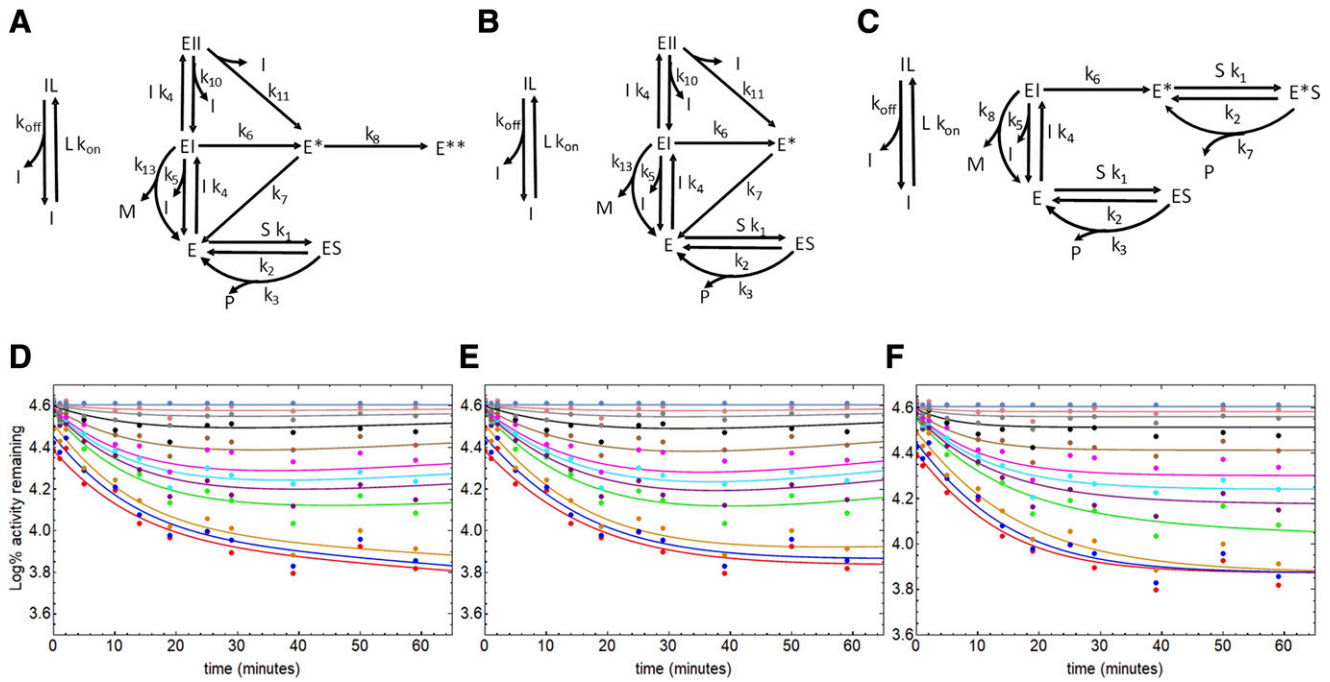


Fig. 8. Kinetic schemes and model fits for CYP2A6 inactivation by CA (1000–0 μM) in HLM. (A) Kinetic scheme for EII-MIC-M-IL model 1. (B) Kinetic scheme for EII-MIC-M-IL model 2. (C) Kinetic scheme for PI-M-IL model. (D) Experimental (points) and EII-MIC-M-IL model fitted (solid lines) PRA plots. (E) Experimental (points) and EII-MIC-M-IL model 2 fitted (solid lines) PRA plots. (F) Experimental (points) and PI-M-IL model fitted (solid lines) PRA plots. The colors indicate different inactivator concentrations: 1000 (red), 750 (blue), 500 (orange), 250 (green), 200 (violet), 175 (cyan), 150 (magenta), 100 (brown), 50 (black), 25 (gray), 12.5 μM (pink), and solvent control (light gray).

function decreased as K_{I2} became smaller such that $K_{I2} \ll K_{I1}$. The double-binding model with partial inactivation and inhibitor depletion gave a better fit than the double-binding model with quasi-irreversible and inhibitor depletion (data not shown). The results for three model fits (MIC-M-IL, PI-M-IL, and EII-PI-M-IL) are shown in Table 3 and Fig. 9.

In summary, for CA, partial inactivation with inhibitor depletion (PI-M-IL) was the best-fit model, followed by double-binding models with MIC and inhibitor depletion (EII-MIC-M-IL), in which PI indicates partial inactivation. For MCA, a double-binding model with partial inactivation along with inhibitor depletion gave the best fit (EII-PI-M-IL). PI occurs when modified enzymes retain residual activity (Crowley and Hollenberg, 1995). EII is double-inhibitor binding, and MIC represents metabolite intermediate complex formation. M and IL indicate inhibitor metabolism and lipid partitioning, respectively.

Microsomal Partitioning of CA and MCA. The predicted $f_{u,mic}$ (0.25 mg/ml) was 0.88 and 0.86 for CA and MCA, respectively.

The predicted $f_{u,mic}$ was scaled to 5 mg/ml using an equation described previously (Kalvass and Maurer, 2002):

$$f_{u,mic} (5\text{mg/ml}) = \frac{\frac{1}{D}}{\left(\frac{1}{f_{u,mic} (0.25\text{mg/ml})} - 1\right) + \frac{1}{D}}$$

where $f_{u,mic}$ (5 mg/ml) is the scaled unbound fraction at 5 mg/ml microsomal protein, and $f_{u,mic}$ (0.25 mg/ml) is the unbound fraction experimentally measured at 0.25 mg/ml. D is the dilution factor of microsomal concentration between 0.25 and 5 mg/ml, which is 20. The predicted $f_{u,p}$ was 0.19 and 0.26 for CA and MCA, respectively.

Herb-Drug Interaction Prediction for Nicotine. HDI predictions were performed using the standard static model as recommended by the FDA (<https://www.fda.gov/media/134582/download>). $K_{I,u}$ and k_{inact} parameters obtained from the PI-M-IL model for CA and EII-PI-M-IL model for MCA were used for HDI predictions. The CYP2A6 half-life of 37 hours was used for the HDI predictions (Renwick et al., 2000). The results for oral dosing are shown in Table 4. The predicted AUC ratios

TABLE 2
In vitro TDI parameter estimates for CA using numerical and replot methods

Parameters	Numerical Method Models			Replot Method
	EII-MIC-M-IL Model 1 ^{a,b}	EII-MIC-M-IL Model 2 ^a	PI-M-IL	
AICc	-528.56	-527.17	-536.42	—
R^2	0.9987	0.9987	0.9988	—
k_{inact} (min^{-1}) ^c	0.003 ± 0.001	0.023 ± 0.012	0.100 ± 0.010	0.025 ± 0.001
$K_{I,u}$ (μM) ^c	$K_{I,u1} = 60.69 \pm 18.47$ $K_{I,u2} = 101.00 \pm 90.29$	$K_{I,u1} = 60.00 \pm 18.06$ $K_{I,u2} = 94.36 \pm 81.09$	37.44 ± 4.15	15.24 ± 3.22

^aTwo binding model.

^b k_{k8} fixed at 0.005 min^{-1} .

^cEstimated value \pm S.E.

TABLE 3
In vitro TDI parameter estimates for MCA using numerical and replot methods

Parameters	Numerical Method Models			Replot Method
	MIC-M-IL	PI-M-IL	EII-PI-M-IL ^a	
AICc	-583.95	-608.48	-636.53	—
R ²	0.9980	0.9983	0.9986	—
k _{inact} (min ⁻¹) ^b	0.022 ± 0.008	0.27 ± 0.06	k ₆ = 0.71 ± 0.15 k ₁₁ = 0.11 ± 0.02	0.16 ± 0.03
K _{I,u} (μM) ^b	K _{I,u} = 38.6 ± 12.63	26.83 ± 8.30	K _{I,u1} = 104.00 ± 27.57 K _{I,u2} = 5 (fixed)	57.15 ± 15.38

^aTwo binding model.

^bEstimated value ± S.E.

for the CA-nicotine and CA-letrozole interactions were 4.29 and 4.92, respectively. The predicted AUC ratios were 4.35 and 5.00 for the MCA-nicotine and MCA-letrozole interactions, respectively. The predicted interaction suggested that substantial exposure to CA and MCA through cinnamon-containing food, cinnamon-flavored products, and the use of cinnamon powder as an herbal treatment can lead to significant interactions with CYP2A6 substrates. Moreover, CYP2A6 is known to be polymorphic (Raunio et al., 2001; McDonagh et al., 2012; Hosono

et al., 2017; Tanner and Tyndale, 2017), which can increase the variability and significance in HDIs (<https://www.pharmvar.org/gene/CYP2A6>). Notably, the fraction metabolized by CYP2A6 can range from 0.60 to 0.77 for nicotine (Benowitz and Jacob, 1994) and ≈0.80 for letrozole (Sioufi et al., 1997; Murai et al., 2009; Chan et al., 2016).

Analysis of CYP2A6 Heme and Search for Heme/Protoporphyrin IX Adducts with MCA and Metabolites of MCA. To investigate the effect of MCA on heme stability, heme was analyzed

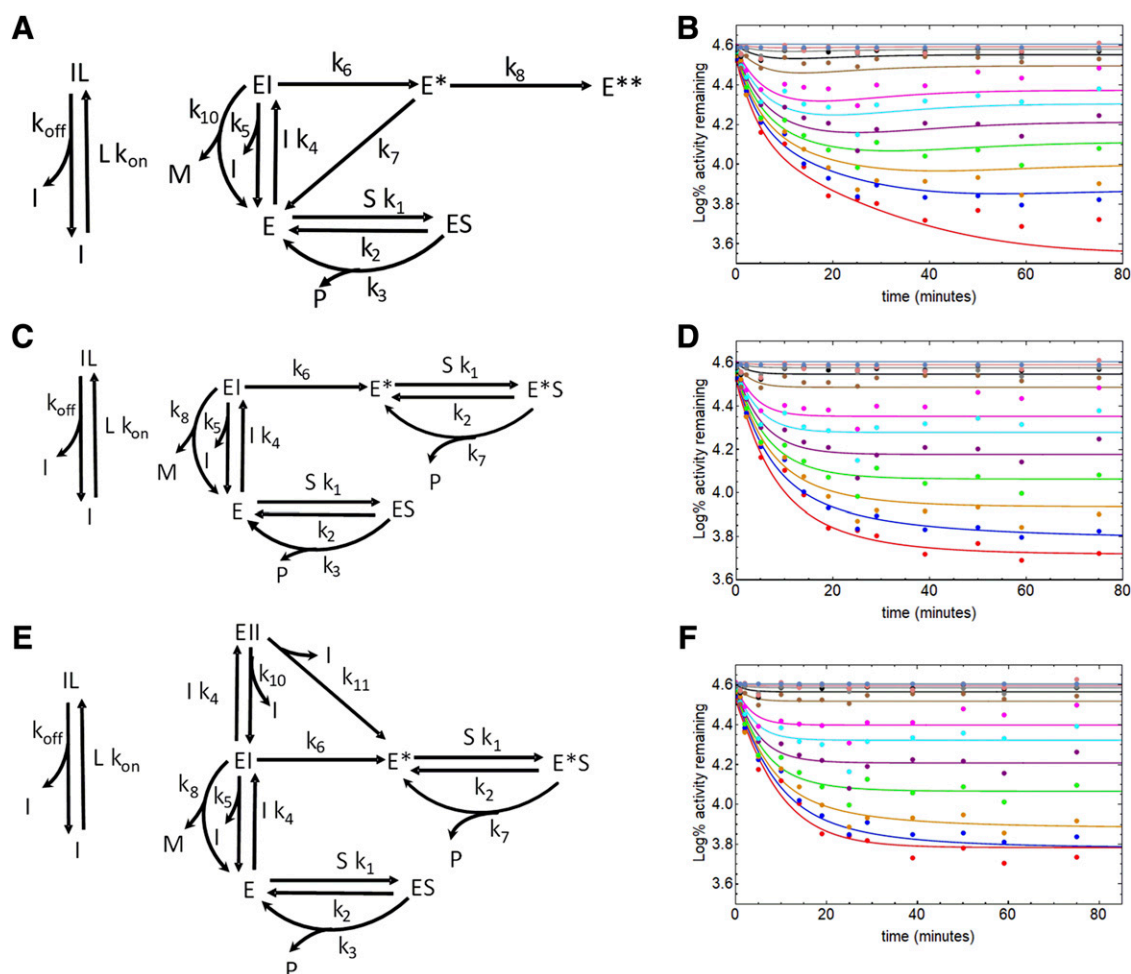


Fig. 9. Kinetic schemes and model fits for CYP2A6 inactivation by MCA (250–0 μM) in HLM. (A) Kinetic scheme for MIC-M-IL model. (B) Experimental (points) and MIC-M-IL model fitted (solid lines) PRA plots. (C) Kinetic scheme for PI-M-IL model. (D) Experimental (points) and PI-M-IL model fitted (solid lines) PRA plots. (E) Kinetic scheme for EII-PI-M-IL model. (F) Experimental (points) and EII-PI-M-IL model fitted (solid lines) PRA plots. The colors indicate different inactivator concentrations: 250 (red), 200 (blue), 175 (orange), 150 (green), 125 (violet), 100 (cyan), 80 (magenta), 40 (brown), 20 (black), 10 (gray), 5 μM (pink), and solvent control (light gray).

TABLE 4

Herb-drug interaction predictions for CA and MCA with nicotine and letrozole using K_{Iu} and k_{inact} obtained using the numerical method and CYP2A6 half-life = 37 h

Substrate	Inhibitor	TDI Parameter Estimation Method	Herb-Drug Interaction Prediction (AUC-Fold Increase)
Nicotine	CA	Replot	4.21
		Numerical	4.29
	MCA	Replot	4.31
		Numerical	4.35
Letrozole	CA	Replot	4.82
		Numerical	4.92
	MCA	Replot	4.94
		Numerical	5.00

after incubation with rCYP2A6 in the presence and absence of MCA and directly measured by LC-MS/MS/UV (616/557 amu; 405 nm). When incubated with MCA and NADPH, 48.5% of the heme peak was lost relative to enzyme-plus-NADPH controls (S.D. = 13.4%; 95% CI = 34.4%–62.6%; $P = 0.0082$; $N = 6$) (Fig. 10). No isolable heme adducts were found with UV or by using a full Q1 scan. In an attempt to identify potential adducts of MCA and its metabolites to heme or protoporphyrin IX, samples were subjected to mass defect filtering. We have used this approach previously to successfully identify benzyne adducts of CYP2A6 from incubations with 1-aminobenzotriazole, a pan inhibitor of cytochrome P450 enzymes (manuscript under review). No adducts of MCA (or metabolites) to the heme or protoporphyrin IX were detected using this approach.

Apoprotein Analysis. The potential for MCA, CA, and/or respective metabolites to form an adduct with CYP2A6 apoprotein was investigated using purified reconstituted enzyme. As 8-MOP is known to form a covalent adduct with the apoprotein of CYP2A6 (Koenigs and Trager, 1998), it was used as a positive control. A comparison of the deconvoluted spectra from each condition indicated that CA, MCA, and 8-MOP all formed a second detectable ion envelope of CYP2A6 (Fig. 11), which indicated that apoprotein modifications were present in each case (Table 5). Incubations with the inhibitors without NADPH also yielded adduct peaks, although smaller in area in comparison with incubations including NADPH. Incubations without inhibitor yielded a single dominant mass for CYP2A6 of $54,467.47 \pm 1.23$ Da, corresponding to the theoretical mass of rCYP2A6. Reductase yielded a main peak of $77,724.02 \pm 4$ Da.

Incubations with MCA yielded an additional mass of $54,622.85 \pm 11.89$ Da near the CYP2A6 peak, whereas incubations with CA yielded an additional mass of $54,600.05 \pm 9.59$ Da. There were no statistically significant additions to the reductase peaks in any case. Incubations were also attempted with 5 mM glutathione ($N = 6$ for each inhibitor). Incubations from these experiments did not yield statistically significant differences from incubations without glutathione, signifying that the reactive metabolites are likely adducting CYP2A6 without leaving the active site. In an attempt to determine whether adduct formation was NADPH-dependent, area ratios of modified CYP2A6 and unmodified CYP2A6 peaks were determined for each incubation condition (Table 5). In the case of both MCA and CA, the peak area ratio—that is, $\text{peak area}_{\text{CYP2A6 mass + inhibitor mass}}/\text{peak area}_{\text{CYP2A6 mass}}$ —was higher in samples containing NADPH than controls without NADPH.

Discussion

Interactions between CYP2A6, MCA, and CA were investigated using a multifaceted approach that was intended to discover mechanistic insights to inform HDI predictions. New information includes a description of MCA-CYP2A6 binding, evidence for the dynamic nature of CA/MCA ligands bound to CYP2A6, and evidence that at least two mechanisms contribute to TDI. Analyzing TDI data with the numerical

analysis method allowed for consideration of multiple mechanisms in estimating k_{inact} and K_{I} , which were used for HDI predictions. The results are discussed in order: 1) binding interactions, 2) TDI mechanisms and parameter estimates, and 3) HDI predictions.

Atypical kinetics (i.e., non-Michaelis-Menten) are widely observed with P450s (Korzekwa et al., 1998; Atkins, 2005; Korzekwa, 2014; Leow and Chan, 2019), which have mechanistically been attributed to multiple binding (Korzekwa et al., 1998), protein heterogeneity (Davydov and Halpert, 2008), enzyme oligomerization, protein-protein interactions (Davydov et al., 2017; Davydova et al., 2019), or a combination. Atypical kinetics can profoundly impact TDI kinetics (Korzekwa et al., 2014; Nagar et al., 2014), and evidence suggests that DDI predictions can be improved by accounting for mechanistic complexities (Yadav et al., 2018).

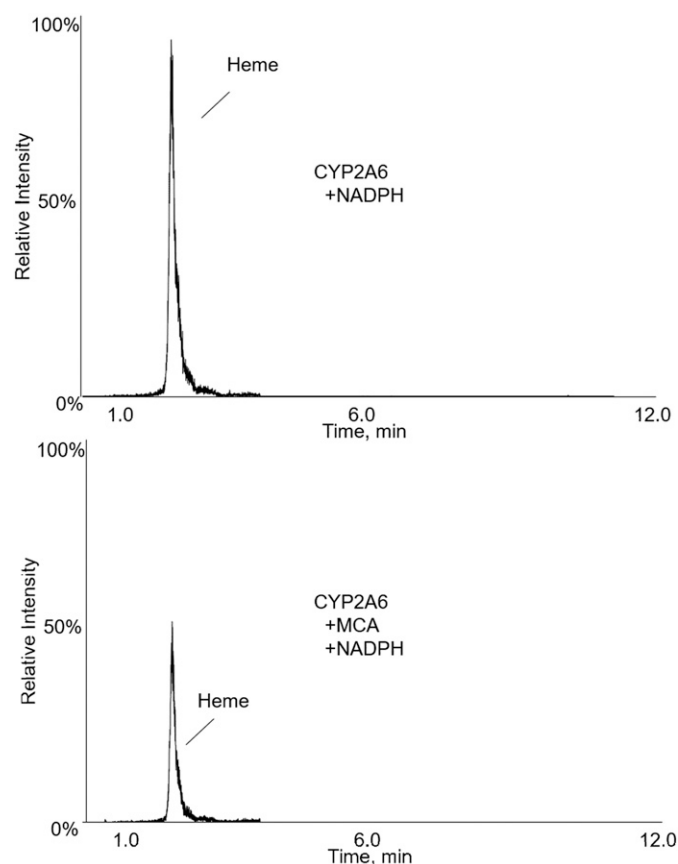


Fig. 10. Representative LC-MS/MS traces showing detection of heme from incubations of rCYP2A6 with NADPH (top panel) and rCYP2A6 with MCA and NADPH (bottom panel). Incubations with MCA and NADPH exhibited a 48.5% heme loss relative to enzyme-plus-NADPH controls (S.D. = 13.4%; 95% CI = 34.4%–62.6%; $P = 0.0082$; $N = 6$).

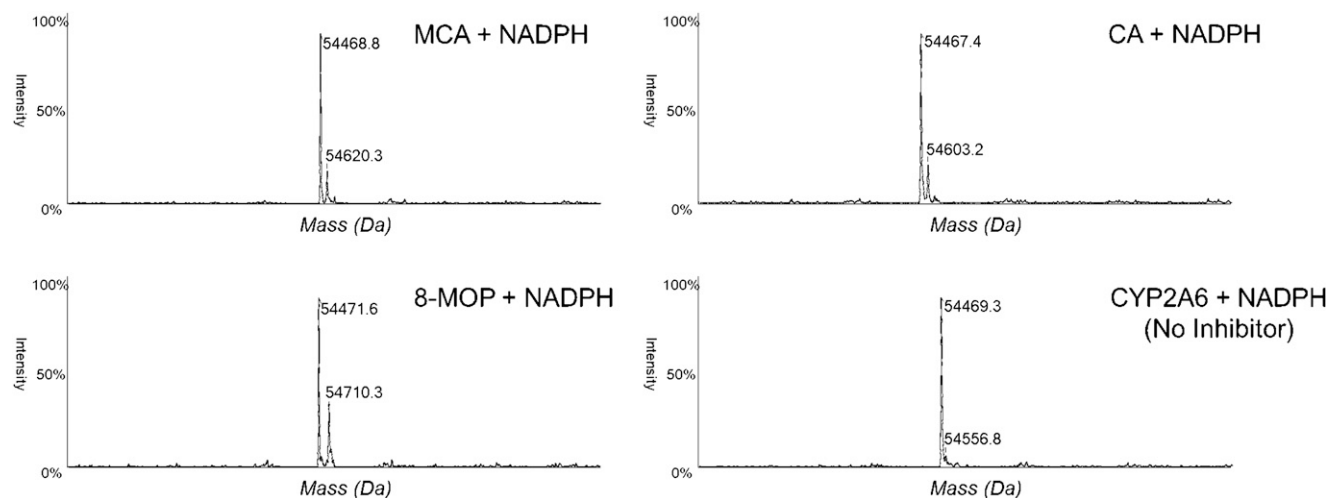


Fig. 11. Masses of CYP2A6 from incubations containing MCA (top left), 8-MOP (bottom left), CA (top right), or no inhibitor (bottom right). Main peaks indicate the unmodified CYP2A6 mass, and minor peaks indicate possible adducts. Deconvolution was achieved by extracting the spectra around the vertex of the peak at the retention time of CYP2A6 and processed using the Biotoolkit add-on in the PeakView software (AB Sciex).

CYP2A6 and CYP2E1 have more restricted active site volumes among human P450s (DeVore et al., 2008; Porubsky et al., 2008); yet there is evidence both enzymes accommodate multiple ligands simultaneously and exhibit homotropic and heterotropic allosteric behavior (Harrelson et al., 2008; Hartman et al., 2012, 2013, 2015). Spectral binding analysis can provide evidence for multiple-ligand binding; it may also overlook some multiple-ligand binding scenarios, as the binding of a second ligand may not always generate changes in the spin state of the heme iron (Davydov et al., 2002; Atkins, 2005). Here, the spectral binding data for MCA fit best to a model that allows for multiple-ligand binding (Hill coefficient >1). The binding data were consistent with results from the numerical method, in which a double-inhibitor model (E•I•I) fit best to the kinetic data. MCA ($K_S = 1.6 \mu\text{M}$) binds with greater affinity than CA to CYP2A6 ($K_S = 14.9 \mu\text{M}$), which was found previously to fit best to a one-site binding model (Chan et al., 2016). Notably, here, the numerical method analysis of the CA TDI data set fit best to a single-inhibitor model.

Although MCA binds with greater affinity than CA, there were some similarities in binding dynamics. MD simulations investigated both single- (E•I) and double-ligand (E•I•I) binding scenarios. In both scenarios, the ligand closest to the heme exhibited two predominant orientations: one with the aldehyde carbonyl oriented to the heme iron (position I) and another with the aromatic ring near the heme iron (position II). Hydrogen bonds with N297 were important in stabilizing the ligand orientations, similar to previous observations (DeVore et al., 2008, 2009). The MD results showed that the CYP2A6 active site is adequately voluminous to accommodate two ligands and that

simultaneous binding of two CA or two MCA molecules is possible. The MD results also showed that both inhibitors are dynamic within the active site, and the binding of a second ligand to form the E•I•I complex stabilized the structure of the ligand closest to the heme.

The overall observation that ligand binding is dynamic suggests multiple atoms on the same ligand will be exposed to the active oxidizing species and is consistent with the CYP2A6-mediated metabolism of CA and MCA. For MCA, three metabolic routes were identified: *O*-demethylation, aromatic hydroxylation, and epoxidation. A predominant binding position for MCA places the aromatic ring in close proximity to the heme iron (i.e., position II; Fig. 4B; Fig. 6B), a favorable position for aromatic hydroxylation and demethylation. Transitory positions that occur as MCA reorients between positions I and II expose the double bond, between the α,β -carbons, to the active oxidizing species, allowing for epoxidation. For CA and MCA, both single-ligand binding and E•I•I also result in orientations in which the carbonyl carbon is in close proximity to the heme (position I). For CA, this is consistent with metabolism studies in which cinnamic acid was the only detectable metabolite (manuscript under review). The metabolism studies were conducted at a saturating substrate concentration to maximize metabolite production. Now that multiple MCA metabolites have been identified, it affords an opportunity to further investigate multiple-ligand binding by evaluating product ratios as a function of MCA concentration.

The accumulated mass spectral evidence supports at least two mechanisms for CYP2A6 inactivation by both CA and MCA: heme degradation and apoprotein modification. Simultaneous modification of

TABLE 5

Mass additions to CYP2A6 apoprotein from deconvoluted spectra of samples incubated with MCA, CA, and 8-MOP ($N = 6$ for all conditions)

Incubation Conditions	Theoretical Mass (Da)	Measured Mass (Da)	95% CI	Peak Area Ratio Adducted 2A6/2A6 ^a	95% CI
MCA + NADPH	162.19	156.79	142.54–171.04	0.24 ^b	0.15–0.32
MCA – NADPH	162.19	151.66	136.88–166.44	0.13	–0.001 to 0.14
CA + NADPH	132.16	132.67	123.37–141.98	0.26 ^b	0.14–0.37
CA – NADPH	132.16	127.61	118.56–136.65	0.13	0.07–0.18
8-MOP + NADPH	216.19 232.19	247.97	235.70–260.24	0.59	0.42–0.75
2A6 + NADPH ^c	N/A	N/A	N/A	N/A	N/A

^aPeak area_(CYP2A6 mass + inhibitor mass)/peak area_(CYP2A6 mass)

^b $P = 0.003$ (MCA); $P = 0.025$ (CA); comparison with CYP2A6 with inhibitor minus NADPH.

^cN/A indicates 'not applicable' as a deconvoluted peak corresponding to covalently modified CYP2A6 was not observed in these samples.

heme and apoprotein was observed previously with bergamottin (He et al., 1998; Lin et al., 2005), mifepristone (Lin et al., 2009), and clopidogrel (Zhang et al., 2011). Substantial NADPH-dependent heme loss was observed in the presence of MCA (Fig. 10). Studies of CYP2B4 inactivation by 3-phenylpropionaldehyde, a structural analog of CA, showed evidence of heme adducts with a deformed metabolite of 3-phenylpropionaldehyde (Kuo et al., 1999). If heme adducts are formed with MCA metabolites, they may be unstable with the conditions used here. Heme loss without detectable heme adducts has also been observed with CA (manuscript under review) as well as loss of CO binding (Chan et al., 2016). The previous evidence that heme adduction/degradation involves the carbonyl of phenylpropanoids may explain the absence of 2-methoxycinnamic acid as a detectable metabolite of MCA. When MCA is metabolized by CYP2A6 at the carbonyl position, heme degradation may be more favored than carboxylic acid metabolite formation.

CA and MCA form covalent adducts with CYP2A6 apoprotein through catalytic and noncatalytic processes, although metabolism enhanced adduction, as modification was maximal with NADPH. Although the variability for the deconvoluted spectra precludes determining exact masses of the adducts, the measured masses and 95% CI (Table 5) suggest structures with molecular weights that are close to the parent masses, CA (mol. wt. 132.16) and MCA (mol. wt. 162.19), without the addition of oxygen. Noncatalytic modification through Michael addition and/or Schiff base formation (Prakash et al., 2008; Chan et al., 2016) would generate adducts similar to the detected masses. For catalytically driven modification, a multistep process would result in the observed adducts: 1) epoxidation between the α,β -carbons; 2) reaction with a nucleophilic residue (e.g., cysteine) to open the epoxide; and 3) dehydration to eliminate water, regenerating the double bond (Niklasson et al., 2014). Notably, epoxide metabolites trapped as glutathione conjugates were identified for MCA (mol. wt. 162) and demethylated MCA (mol. wt. 150), intimating that epoxides are formed from both the parent compound and demethylated metabolite. If both epoxides react with CYP2A6 residues similar to reactions with glutathione, this could explain both why the detected adduct mass was ≈ 156 (the average of 162 and 150) and the greater variability observed for MCA versus CA. Although glutathione did not change the formation of apoprotein adducts for either inhibitor, it is possible that other nucleophilic trapping agents (e.g., methoxylamine, *N*-acetyllysine, semicarbide, potassium cyanide) may capture the reactive metabolites.

The numerical method allows for diverse mechanistic factors to be considered when estimating TDI parameters. CYP2A6 inactivation data were evaluated using several models (>15) that combined different kinetic events, such as inhibitor depletion, quasi-irreversible (MIC) formation, partial inactivation, lipid partitioning, and multiple binding. Consistent with MD simulations, results from the numerical method analysis exhibited support for multiple inactivator binding to CYP2A6 for both CA and MCA. Further, the concave upward curvature in the PRA plots suggested either partial inactivation or quasi-irreversible inactivation. The mass spectral evidence showed heme loss and apoprotein modification as potential contributors to inhibition for both compounds. Apoprotein modification can lead to partial inactivation wherein the enzyme still possesses activity, albeit lower than the unmodified enzyme (Crowley and Hollenberg, 1995).

For both CA and MCA, quasi-irreversible (MIC formation) and partial inactivation models were evaluated. The partial inactivation models with inhibitor depletion (PI-M-IL) resulted in better fits for both inhibitors. CA and MCA do not possess functional groups typically associated with MIC (e.g., amines, methylenedioxy aromatics) (Kalgutkar et al., 2007; Kamel and Harriman, 2013; Mohutsky and Hall, 2014; Limban et al., 2018). For MCA, a divergence between K_i and K_i

suggested multiple binding kinetics (Korzekwa et al., 2014; Nagar et al., 2014). Analysis of the PRA graphs (linear portions) using the standard replot method suggested biphasic kinetics with lack of saturation for the second binding. In general, it is difficult to estimate K_{12} when inhibitor solubility prevents enzyme saturation. The kinetics of MCA inactivation are complex and might require more data for complete parameterization. In summary, the combined results point toward an inactivation process that involves multiple inhibitor binding, inhibitor depletion, and partial inactivation.

Although clinical data are lacking for CA and MCA, an effort was made to predict an HDI with parameters scaled from rats. The exposure range for CA is estimated to be between 8 and 275 mg (Friedman et al., 2000; Kirkham et al., 2009; Chan et al., 2016). The prediction used a virtual study design of 275 mg dosed every 24 hours for 10 days. The prediction suggests that extensive exposure to cinnamon—for example, through food or large doses of cinnamon powder as a complementary treatment—would lead to noteworthy interactions (AUC changes > 4-fold) with CYP2A6 substrates (e.g., nicotine, letrozole, and metronidazole).

In summary, the evidence from multiple approaches indicates that the time-dependent inhibition of CYP2A6 by MCA and CA is a complex process involving multiple factors and mechanisms. Both agents are dynamic within the CYP2A6 active site, reorienting between a few preferred orientations. The CYP2A6 active site appears to be sufficiently voluminous and flexible to accommodate two MCA or CA ligands: for MCA, this is especially consistent with results from ligand binding and numerical method analysis. Apoprotein modification, heme degradation, and partial inactivation are observed with both agents. Although MCA is more potent than CA, both are present in cinnamon, and questions remain as to how one agent may modulate the inhibition potency and metabolism of the other (e.g., heterotropic effects). Furthermore, factors that influence the relative partitioning between heme degradation, apoprotein modification, and metabolite formation are unknown. Based on this study, individuals taking CYP2A6 substrates, such as nicotine (e.g., self-administration through smoking, vaping, nicotine replacement therapy) and ingesting large quantities of cinnamon may be at risk of increased exposure to the CYP2A6 substrate through HDI resulting from CA and/or MCA.

Authorship Contributions

Participated in research design: Espiritu, Yadav, Pelletier, Chan, Natesan, Harrelson.

Conducted experiments: Espiritu, Chen, Yadav, Larkin, Pelletier, Harrelson.

Performed data analysis: Espiritu, Chen, Yadav, Larkin, Pelletier, Chan, GC, Natesan, Harrelson.

Wrote or contributed to the writing of the manuscript: Espiritu, Chen, Yadav, Larkin, Pelletier, Chan, GC, Natesan, Harrelson.

References

- Molecular Operating Environment (MOE) 2013.08. Montreal, QC, Canada, Chemical Computing Group ULC.
- Akaike H (1974) A new look at the statistical model identification. *IEEE Trans Automat Contr* **19**: 716–723.
- Akilen R, Tsiami A, Devendra D, and Robinson N (2010) Glycated haemoglobin and blood pressure-lowering effect of cinnamon in multi-ethnic Type 2 diabetic patients in the UK: a randomized, placebo-controlled, double-blind clinical trial. *Diabet Med* **27**:1159–1167.
- Atkins WM (2005) Non-Michaelis-Menten kinetics in cytochrome P450-catalyzed reactions. *Annu Rev Pharmacol Toxicol* **45**:291–310.
- Baer BR, Wieners LC, and Rock DA (2007) Time-dependent inactivation of P450 3A4 by raloxifene: identification of Cys239 as the site of apoprotein alkylation. *Chem Res Toxicol* **20**: 954–964.
- Barnaba C, Yadav J, Nagar S, Korzekwa K, and Jones JP (2016) Mechanism-based inhibition of CYP3A4 by podophyllotoxin: aging of an intermediate is important for in vitro/in vivo correlations. *Mol Pharm* **13**:2833–2843.
- Behar RZ, Luo W, Lin SC, Wang Y, Valle J, Pankow JF, and Talbot P (2016) Distribution, quantification and toxicity of cinnamaldehyde in electronic cigarette refill fluids and aerosols. *Tob Control* **25** (Suppl 2):ii94–ii102.

- Behar RZ, Luo W, McWhirter KJ, Pankow JF, and Talbot P (2018) Analytical and toxicological evaluation of flavor chemicals in electronic cigarette refill fluids. *Sci Rep* **8**:8288.
- Benowitz NL and Jacob P III (1994) Metabolism of nicotine to cotinine studied by a dual stable isotope method. *Clin Pharmacol Ther* **56**:483–493.
- Brandänge S and Lindblom L (1979) The enzyme “aldehyde oxidase” is an iminium oxidase. Reaction with nicotine delta 1'(5') iminium ion. *Biochem Biophys Res Commun* **91**:991–996.
- Burgess G and Williams D (2010) The discovery and development of analgesics: new mechanisms, new modalities. *J Clin Invest* **120**:3753–3759.
- Caldwell GW, Masucci JA, Yan Z, and Hageman W (2004) Allometric scaling of pharmacokinetic parameters in drug discovery: can human CL, Vss and t1/2 be predicted from in-vivo rat data? *Eur J Drug Metab Pharmacokinet* **29**:133–143.
- Cao H, Sethumadhavan K, Li K, Boue SM, and Anderson RA (2019) Cinnamon polyphenol extract and insulin regulate diacylglycerol acyltransferase gene expression in mouse adipocytes and macrophages. *Plant Foods Hum Nutr* **74**:115–121.
- Chan J, Oshiro T, Thomas S, Higa A, Black S, Todorovic A, Elbarby F, and Harrelson JP (2016) Inactivation of CYP2A6 by the dietary phenylpropanoid trans-cinnamic aldehyde (cinnamaldehyde) and estimation of interactions with nicotine and letrozole. *Drug Metab Dispos* **44**:534–543.
- Cheng WX, Zhong S, Meng XB, Zheng NY, Zhang P, Wang Y, Qin L, and Wang XL (2020) Cinnamaldehyde inhibits inflammation of human synovial cells through regulation of Jak/Stat pathway and ameliorates collagen-induced arthritis in rats. *J Pharmacol Exp Ther* **373**:302–310.
- Cleland WW (1975) Partition analysis and the concept of net rate constants as tools in enzyme kinetics. *Biochemistry* **14**:3220–3224.
- Crawford P (2009) Effectiveness of cinnamon for lowering hemoglobin A1C in patients with type 2 diabetes: a randomized, controlled trial. *J Am Board Fam Med* **22**:507–512.
- Crowley JR and Hollenberg PF (1995) Mechanism-based inactivation of rat liver cytochrome P4502B1 by phenylcyclidine and its oxidative product, the iminium ion. *Drug Metab Dispos* **23**:786–793.
- Davies B and Morris T (1993) Physiological parameters in laboratory animals and humans. *Pharm Res* **10**:1093–1095.
- Davydov DR, Davydova NY, Rodgers JT, Rushmore TH, and Jones JP (2017) Toward a systems approach to the human cytochrome P450 ensemble: interactions between CYP2D6 and CYP2E1 and their functional consequences. *Biochem J* **474**:3523–3542.
- Davydov DR and Halpert JR (2008) Allosteric P450 mechanisms: multiple binding sites, multiple conformers or both? *Expert Opin Drug Metab Toxicol* **4**:1523–1535.
- Davydov DR, Kumar S, and Halpert JR (2002) Allosteric mechanisms in P450eryF probed with 1-pyrenebutanol, a novel fluorescent substrate. *Biochem Biophys Res Commun* **294**:806–812.
- Davydova NY, Dangi B, Maldonado MA, Vavilov NE, Zgoda VG, and Davydov DR (2019) Toward a systems approach to cytochrome P450 ensemble: interactions of CYP2E1 with other P450 species and their impact on CYP1A2. *Biochem J* **476**:3661–3685.
- DeVore NM, Smith BD, Urban MJ, and Scott EE (2008) Key residues controlling phenacetin metabolism by human cytochrome P450 2A enzymes. *Drug Metab Dispos* **36**:2582–2590.
- DeVore NM, Smith BD, Wang JL, Lushington GH, and Scott EE (2009) Key residues controlling binding of diverse ligands to human cytochrome P450 2A enzymes. *Drug Metab Dispos* **37**:1319–1327.
- Feller SE, Zhang YH, Pastor RW, and Brooks BR (1995) Constant-pressure molecular-dynamics simulation - the Langevin piston method. *J Chem Phys* **103**:4613–4621.
- Foti RS, Rock DA, Pearson JT, Wahlstrom JL, and Wienkers LC (2011) Mechanism-based inactivation of cytochrome P450 3A4 by mibefradil through heme destruction. *Drug Metab Dispos* **39**:1188–1195.
- Friedman M, Kozukue N, and Harden LA (2000) Cinnamaldehyde content in foods determined by gas chromatography-mass spectrometry. *J Agric Food Chem* **48**:5702–5709.
- Gao H, Yao L, Mathieu HW, Zhang Y, Maurer TS, Troutman MD, Scott DO, Ruggeri RB, and Lin J (2008) In silico modeling of nonspecific binding to human liver microsomes. *Drug Metab Dispos* **36**:2130–2135.
- Guengerich FP, Martin MV, Sohl CD, and Cheng Q (2009) Measurement of cytochrome P450 and NADPH-cytochrome P450 reductase. *Nat Protoc* **4**:1245–1251.
- Hagenlocher Y, Hösel A, Bischoff SC, and Lorentz A (2016) Cinnamon extract reduces symptoms, inflammatory mediators and mast cell markers in murine IL-10(-/-) colitis. *J Nutr Biochem* **30**:85–92.
- Harrelson JP, Atkins WM, and Nelson SD (2008) Multiple-ligand binding in CYP2A6: probing mechanisms of cytochrome P450 cooperativity by assessing substrate dynamics. *Biochemistry* **47**:2978–2988.
- Harrelson JP, Stamper BD, Chapman JD, Goodlett DR, and Nelson SD (2012) Covalent modification and time-dependent inhibition of human CYP2E1 by the meta-isomer of acetaminophen. *Drug Metab Dispos* **40**:1460–1465.
- Hartman JH, Boysen G, and Miller GP (2012) CYP2E1 metabolism of styrene involves allostery. *Drug Metab Dispos* **40**:1976–1983.
- Hartman JH, Boysen G, and Miller GP (2013) Cooperative effects for CYP2E1 differ between styrene and its metabolites. *Xenobiotica* **43**:755–764.
- Hartman JH, Letzig LG, Roberts DW, James LP, Fifer EK, and Miller GP (2015) Cooperativity in CYP2E1 metabolism of acetaminophen and styrene mixtures. *Biochem Pharmacol* **97**:341–349.
- He K, Iyer KR, Hayes RN, Sinz MW, Woolf TF, and Hollenberg PF (1998) Inactivation of cytochrome P450 3A4 by bergamottin, a component of grapefruit juice. *Chem Res Toxicol* **11**:252–259.
- Hosono H, Kumondai M, Maekawa M, Yamaguchi H, Mano N, Oda A, Hirasawa N, and Hiratsuka M (2017) Functional characterization of 34 CYP2A6 allelic variants by assessment of nicotine C-oxidation and coumarin 7-hydroxylation activities. *Drug Metab Dispos* **45**:279–285.
- Huang J and MacKerell AD Jr. (2013) CHARMM36 all-atom additive protein force field: validation based on comparison to NMR data. *J Comput Chem* **34**:2135–2145.
- Hukkanen J, Jacob P III, and Benowitz NL (2005) Metabolism and disposition kinetics of nicotine. *Pharmacol Rev* **57**:9–115.
- Jorgensen WL, Chandrasekhar J, Madura JD, Impey RW, and Klein ML (1983) Comparison of simple potential functions for simulating liquid water. *J Chem Phys* **79**:926–935.
- Kalgtkar AS, Obach RS, and Maurer TS (2007) Mechanism-based inactivation of cytochrome P450 enzymes: chemical mechanisms, structure-activity relationships and relationship to clinical drug-drug interactions and idiosyncratic adverse drug reactions. *Curr Drug Metab* **8**:407–447.
- Kalvass JC and Maurer TS (2002) Influence of nonspecific brain and plasma binding on CNS exposure: implications for rational drug discovery. *Biopharm Drug Dispos* **23**:327–338.
- Kamel A and Harriman S (2013) Inhibition of cytochrome P450 enzymes and biochemical aspects of mechanism-based inactivation (MBI). *Drug Discov Today Technol* **10**:e177–e189.
- Kirkham S, Akilen R, Sharma S, and Tsiami A (2009) The potential of cinnamon to reduce blood glucose levels in patients with type 2 diabetes and insulin resistance. *Diabetes Obes Metab* **11**:1100–1113.
- Koenigs LL and Trager WF (1998) Mechanism-based inactivation of P450 2A6 by furanocoumarins. *Biochemistry* **37**:10047–10061.
- Korzekwa K (2014) Enzyme kinetics of oxidative metabolism: cytochromes. *Enzyme Kinetics in Drug Metabolism* pp 149–166, Springer Science, Humana Press, Totowa, NJ.
- Korzekwa K, Tweedie D, Argikar UA, Whitcher-Johnstone A, Bell L, Bickford S, and Nagar S (2014) A numerical method for analysis of in vitro time-dependent inhibition data. Part 2. Application to experimental data. *Drug Metab Dispos* **42**:1587–1595.
- Korzekwa KR, Krishnamachary N, Shou M, Ogai A, Parise RA, Rettie AE, Gonzalez FJ, and Tracy TS (1998) Evaluation of atypical cytochrome P450 kinetics with two-substrate models: evidence that multiple substrates can simultaneously bind to cytochrome P450 active sites. *Biochemistry* **37**:4137–4147.
- Kundu M, Mondal S, Roy A, Martinson JL, and Pahan K (2016) Sodium benzoate, a food additive and a metabolite of cinnamon, enriches regulatory T cells via STAT6-mediated upregulation of TGF- β . *J Immunol* **197**:3099–3110.
- Kuo CL, Raner GM, Vaz AD, and Coon MJ (1999) Discrete species of activated oxygen yield different cytochrome P450 heme adducts from aldehydes. *Biochemistry* **38**:10511–10518.
- Lee J, Cheng X, Swails JM, Yeom MS, Eastman PK, Lemkul JA, Wei S, Buckner J, Jeong JC, Qi Y, et al. (2016) CHARMM-GUI input generator for NAMD, GROMACS, AMBER, OpenMM, and CHARMM/OpenMM simulations using the CHARMM36 additive force field. *J Chem Theory Comput* **12**:405–413.
- Le Gal A, Dréano Y, Lucas D, and Berthou F (2003) Diversity of selective environmental substrates for human cytochrome P450 2A6: alkoxyethers, nicotine, coumarin, N-nitrosodiethylamine, and N-nitrosobenzylmethylamine. *Cytolet Lett* **144**:77–91.
- Leow JWH and Chan ECY (2019) Atypical Michaelis-Menten kinetics in cytochrome P450 enzymes: a focus on substrate inhibition. *Biochem Pharmacol* **169**:113615.
- Limban C, Nuță DC, Chiriță C, Negreș S, Arsene AL, Goumenou M, Karakitsios SP, Tsatsakis AM, and Sarigiannis DA (2018) The use of structural alerts to avoid the toxicity of pharmaceuticals. *Toxicol Rep* **5**:943–953.
- Lin HL, Kent UM, and Hollenberg PF (2005) The grapefruit juice effect is not limited to cytochrome P450 (P450) 3A4: evidence for bergamottin-dependent inactivation, heme destruction, and covalent binding to protein in P450s 2B6 and 3A5. *J Pharmacol Exp Ther* **313**:154–164.
- Lin HL, Zhang H, and Hollenberg PF (2009) Metabolic activation of mifepristone [RU486; 17 β -hydroxy-11 β -(4-dimethylaminophenyl)-17 α -(1-propynyl)-estra-4,9-dien-3-one] by mammalian cytochromes P450 and the mechanism-based inactivation of human CYP2B6. *J Pharmacol Exp Ther* **329**:26–37.
- Lomize MA, Pogozheva ID, Joo H, Mosberg HI, and Lomize AL (2012) OPM database and PPM web server: resources for positioning of proteins in membranes. *Nucleic Acids Res* **40**:D370–D376.
- McDonagh EM, Wassenaar C, David SP, Tyndale RF, Altman RB, Whirl-Carrillo M, and Klein TE (2012) PharmGKB summary: very important pharmacogene information for cytochrome P-450, family 2, subfamily A, polypeptide 6. *Pharmacogenet Genomics* **22**:695–708.
- Messina ES, Tyndale RF, and Sellers EM (1997) A major role for CYP2A6 in nicotine C-oxidation by human liver microsomes. *J Pharmacol Exp Ther* **282**:1608–1614.
- Mohutsky M and Hall SD (2014) Irreversible enzyme inhibition kinetics and drug-drug interactions. *Methods Mol Biol* **1113**:57–91.
- Monk BC, Tomasiak TM, Keniya MV, Huschmann FU, Tyndall JDA, O'Connell JD III, Cannon RD, McDonald JG, Rodriguez A, Finer-Moore JS, et al. (2014) Architecture of a single membrane spanning cytochrome P450 suggests constraints that orient the catalytic domain relative to a bilayer. *Proc Natl Acad Sci USA* **111**:3865–3870.
- Murai K, Yamazaki H, Nakagawa K, Kawai R, and Kamataki T (2009) Deactivation of anti-cancer drug letrozole to a carbinol metabolite by polymorphic cytochrome P450 2A6 in human liver microsomes. *Xenobiotica* **39**:795–802.
- Murphy PJ (1973) Enzymatic oxidation of nicotine to nicotine 1'(5') iminium ion. A newly discovered intermediate in the metabolism of nicotine. *J Biol Chem* **248**:2796–2800.
- Nagar S, Jones JP, and Korzekwa K (2014) A numerical method for analysis of in vitro time-dependent inhibition data. Part I. Theoretical considerations. *Drug Metab Dispos* **42**:1575–1586.
- Nagar S and Korzekwa K (2017) Drug distribution. Part I. Models to predict membrane partitioning. *Pharm Res* **34**:535–543.
- Nakajima M, Yamamoto T, Nunoya K, Yokoi T, Nagashima K, Inoue K, Funae Y, Shimada N, Kamataki T, and Kuroiwa Y (1996) Role of human cytochrome P4502A6 in C-oxidation of nicotine. *Drug Metab Dispos* **24**:1212–1217.
- Niklasson IB, Ponting DJ, Luthman K, and Karlberg AT (2014) Bioactivation of cinnamic alcohol forms several strong skin sensitizers. *Chem Res Toxicol* **27**:568–575.
- Obach RS, Walsky RL, and Venkatakrishnan K (2007) Mechanism-based inactivation of human cytochrome p450 enzymes and the prediction of drug-drug interactions. *Drug Metab Dispos* **35**:246–255.
- Omura T and Sato R (1962) A new cytochrome in liver microsomes. *J Biol Chem* **237**:1375–1376.
- Omura T and Sato R (1964) The carbon monoxide-binding pigment of liver microsomes. II. Solubilization, purification, and properties. *J Biol Chem* **239**:2379–2385.
- Pahan K (2015) Prospects of cinnamon in multiple sclerosis. *J Mult Scler (Foster City)* **21**:1000149.
- Pang KS and Rowland M (1977) Hepatic clearance of drugs. I. Theoretical considerations of a “well-stirred” model and a “parallel tube” model. Influence of hepatic blood flow, plasma and blood cell binding, and the hepatocellular enzymatic activity on hepatic drug clearance. *J Pharmacokinetic Biopharm* **5**:625–653.
- Pham AQ, Kourlas H, and Pham DQ (2007) Cinnamon supplementation in patients with type 2 diabetes mellitus. *Pharmacotherapy* **27**:595–599.
- Phillips JC, Braun R, Wang W, Gumbart J, Tajkhorshid E, Villa E, Chipot C, Skeel RD, Kalé L, and Schulten K (2005) Scalable molecular dynamics with NAMD. *J Comput Chem* **26**:1781–1802.
- Porubsky PR, Meneely KM, and Scott EE (2008) Structures of human cytochrome P-450 2E1. Insights into the binding of inhibitors and both small molecular weight and fatty acid substrates. *J Biol Chem* **283**:33698–33707.
- Prakash C, Sharma R, Gleave M, and Nedderman A (2008) In vitro screening techniques for reactive metabolites for minimizing bioactivation potential in drug discovery. *Curr Drug Metab* **9**:952–964.

- Ranasinghe P, Pigera S, Premakumara GA, Galappaththy P, Constantine GR, and Katulanda P (2013) Medicinal properties of 'true' cinnamon (*Cinnamomum zeylanicum*): a systematic review. *BMC Complement Altern Med* **13**:275.
- Raner GM, Chiang EW, Vaz AD, and Coon MJ (1997) Mechanism-based inactivation of cytochrome P450 2B4 by aldehydes: relationship to aldehyde deformylation via a peroxyhemiacetal intermediate. *Biochemistry* **36**:4895–4902.
- Raunio H, Rautio A, Gullstén H, and Pelkonen O (2001) Polymorphisms of CYP2A6 and its practical consequences. *Br J Clin Pharmacol* **52**:357–363.
- Renwick AB, Watts PS, Edwards RJ, Barton PT, Guyonnet I, Price RJ, Tredger JM, Pelkonen O, Boobis AR, and Lake BG (2000) Differential maintenance of cytochrome P450 enzymes in cultured precision-cut human liver slices. *Drug Metab Dispos* **28**:1202–1209.
- Rietjens IMCM, Cohen SM, Eisenbrand G, Fukushima S, Gooderham NJ, Guengerich FP, Hecht SS, Rosol TJ, Davidsons JM, Harman CL, et al. (2020) FEMA GRAS assessment of natural flavor complexes: Cinnamomum and Myroxylon-derived flavoring ingredients. *Food Chem Toxicol* **135**:110949.
- Rodgers JT, Davydova NY, Paragas EM, Jones JP, and Davydov DR (2018) Kinetic mechanism of time-dependent inhibition of CYP2D6 by 3,4-methylenedioxymethamphetamine (MDMA): functional heterogeneity of the enzyme and the reversibility of its inactivation. *Biochem Pharmacol* **156**:86–98.
- Rodgers T and Rowland M (2006) Physiologically based pharmacokinetic modelling 2: predicting the tissue distribution of acids, very weak bases, neutrals and zwitterions. *J Pharm Sci* **95**:1238–1257.
- Rostami-Hodjegan A and Tucker G (2004) 'In silico' simulations to assess the 'in vivo' consequences of 'in vitro' metabolic drug-drug interactions. *Drug Discov Today Technol* **1**:441–448.
- Ryckaert J-P, Ciccotti G, and Berendsen HJC (1977) Numerical integration of the cartesian equations of motion of a system with constraints: molecular dynamics of n-alkanes. *J Comput Phys* **23**:327–341.
- Šali A and Blundell TL (1993) Comparative protein modelling by satisfaction of spatial restraints. *J Mol Biol* **234**:779–815.
- Schink A, Naumoska K, Kitanovski Z, Kampf CJ, Fröhlich-Nowoisky J, Thines E, Pöschl U, Schuppan D, and Lucas K (2018) Anti-inflammatory effects of cinnamon extract and identification of active compounds influencing the TLR2 and TLR4 signaling pathways. *Food Funct* **9**:5950–5964.
- Shen AL, Porter TD, Wilson TE, and Kasper CB (1989) Structural analysis of the FMN binding domain of NADPH-cytochrome P-450 oxidoreductase by site-directed mutagenesis. *J Biol Chem* **264**:7584–7589.
- Silverman RB (1995) Mechanism-based enzyme inactivators. *Methods Enzymol* **249**:240–283.
- Sioufi A, Gauducheau N, Pineau V, Marfil F, Jaouen A, Cardot JM, Godbillon J, Czendlik C, Howald H, Pfister C, et al. (1997) Absolute bioavailability of letrozole in healthy postmenopausal women. *Biopharm Drug Dispos* **18**:779–789.
- Stephens ES, Walsh AA, and Scott EE (2012) Evaluation of inhibition selectivity for human cytochrome P450 2A enzymes. *Drug Metab Dispos* **40**:1797–1802.
- Tang H, Hussain A, Leal M, Mayersohn M, and Fluhler E (2007) Interspecies prediction of human drug clearance based on scaling data from one or two animal species. *Drug Metab Dispos* **35**:1886–1893.
- Tanner J-A and Tyndale RF (2017) Variation in CYP2A6 activity and personalized medicine. *J Pers Med* **7**:18.
- Ulrich E, Lalith P, Max LB, Tom D, Hsing L, and Lee GP (1995) A smooth particle mesh Ewald method. *J Chem Phys* **103**:8577–8593.
- Vanommeslaeghe K, Hatcher E, Acharya C, Kundu S, Zhong S, Shim J, Darian E, Guvench O, Lopes P, Vorobyov I, et al. (2010) CHARMM general force field: a force field for drug-like molecules compatible with the CHARMM all-atom additive biological force fields. *J Comput Chem* **31**:671–690.
- Vanommeslaeghe K and MacKerell AD Jr. (2012) Automation of the CHARMM General Force Field (CGenFF) I: bond perception and atom typing. *J Chem Inf Model* **52**:3144–3154.
- Vanommeslaeghe K, Raman EP, and MacKerell AD Jr. (2012) Automation of the CHARMM General Force Field (CGenFF) II: assignment of bonded parameters and partial atomic charges. *J Chem Inf Model* **52**:3155–3168.
- Webb B and Sali A (2016) Comparative protein structure modeling using MODELLER. *Curr Protoc Bioinformatics* **54**:5.6.1–5.6.37.
- Wenzel J, Matter H, and Schmidt F (2019) Predictive multitask deep neural network models for ADME-Tox properties: learning from large data sets. *J Chem Inf Model* **59**:1253–1268.
- Weyer-Menkhoff I and Lötsch J (2018) Human pharmacological approaches to TRP-ion-channel-based analgesic drug development. *Drug Discov Today* **23**:2003–2012.
- Weyer-Menkhoff I and Lötsch J (2019) TRPA1 sensitization produces hyperalgesia to heat but not to cold stimuli in human volunteers. *Clin J Pain* **35**:321–327.
- Yadav J, Korzekwa K, and Nagar S (2018) Improved predictions of drug-drug interactions mediated by time-dependent inhibition of CYP3A. *Mol Pharm* **15**:1979–1995.
- Yadav J, Korzekwa K, and Nagar S (2019) Impact of lipid partitioning on the design, analysis, and interpretation of microsomal time-dependent inactivation. *Drug Metab Dispos* **47**:732–742.
- Yadav J, Paragas E, Korzekwa K, and Nagar S (2020) Time-dependent enzyme inactivation: numerical analyses of in vitro data and prediction of drug-drug interactions. *Pharmacol Ther* **206**:107449.
- Yamazaki H, Inoue K, Hashimoto M, and Shimada T (1999) Roles of CYP2A6 and CYP2B6 in nicotine C-oxidation by human liver microsomes. *Arch Toxicol* **73**:65–70.
- Yang J, Liao M, Shou M, Jamei M, Yeo KR, Tucker GT, and Rostami-Hodjegan A (2008) Cytochrome p450 turnover: regulation of synthesis and degradation, methods for determining rates, and implications for the prediction of drug interactions. *Curr Drug Metab* **9**:384–394.
- Yano JK, Hsu M-H, Griffin KJ, Stout CD, and Johnson EF (2005) Structures of human microsomal cytochrome P450 2A6 complexed with coumarin and methoxsalen. *Nat Struct Mol Biol* **12**:822–823.
- Yokoyama T, Ohbuchi T, Saito T, Sudo Y, Fujihara H, Minami K, Nagatomo T, Uezono Y, and Ueta Y (2011) Allyl isothiocyanates and cinnamaldehyde potentiate miniature excitatory postsynaptic inputs in the supraoptic nucleus in rats. *Eur J Pharmacol* **655**:31–37.
- Yuan JH, Dieter MP, Bucher JR, and Jameson CW (1992) Toxicokinetics of cinnamaldehyde in F344 rats. *Food Chem Toxicol* **30**:997–1004.
- Zhang H, Amunugama H, Ney S, Cooper N, and Hollenberg PF (2011) Mechanism-based inactivation of human cytochrome P450 2B6 by clopidogrel: involvement of both covalent modification of cysteinyl residue 475 and loss of heme. *Mol Pharmacol* **80**:839–847.

Address correspondence to: Dr. John P. Harrelson, School of Pharmacy, Pacific University Oregon, 222 SE 8th Ave., Ste 451, Hillsboro, OR 97123. E-mail: harrelsonj@pacificu.edu
